Phase Field Crystal Models of Quasicrystals

Master's Thesis in Physics

submitted by

Benedikt Decker

December 7, 2017

Institut für Theoretische Physik I
Friedrich-Alexander-Universität Erlangen-Nürnberg

supervised by Prof. Dr. Michael Schmiedeberg

Abstract

Understanding the formation of micro-structures often involves computer simulations. With present-day computers, common methods like molecular dynamics (MD) are limited in timespan, lengthscale and number of particles they can handle. Phase field crystal (PFC) models employing a Swift-Hohenberg-like free energy constitute a computationally efficient alternative for studying crystal structures and their dynamics. They use a coarse-grained free energy expansion with respect to a scalar field that can be associated with a particle density and are widely used to explore the formation of periodic patterns.

It is known that by modifying the phase field crystal model to include a second preferred length scale, quasicrystalline structures can be obtained. Quasicrystals are structures with long-range order that are not periodic in physical space. Most computational discoveries of quasicrystals so far are restricted to 2-dimensional physical space.

In this thesis the phase field crystal model for quasicrystals is extended to 3-dimensional space. A rough overview of the phase diagram of the extended phase field crystal model in three dimensions is given. Among the versatile zoo of different stable and metastable phases in three dimensions, two 2-dimensional stacked quasicrystalline phases have been found. Furthermore it is demonstrated that various different methods which are successfully applied in 2-dimensional simulations are not sufficient to grow stable structures with icosahedral symmetry.

Zusammenfassung

Computersimulationen tragen viel zum Verständnis von Wachstum und Selbstorganisation von Mirkostrukturen bei. Traditionelle Methoden wie Molekulardynamiksimulationen (MD) sind eingeschränkt bezüglich der möglichen Zeiträume, Lägenskalen und Teilchenzahlen, die sich mit aktuellen Computern simulieren lassen. Phasenfeldkristallmodelle (PFC) mit einer Swift-Hohenberg-ähnlichen Freien Energie und Dynamik sind eine recheneffizientere Alternative. Sie verwenden eine grobkörnige Entwicklung der Freien Energie bezüglich eines Ordnungsparameters, der sich als Teilchendichte interpretieren lässt.

Es ist bekannt, dass durch Erweiterung des Phasenfeldkristallmodells um eine zweite bevorzugte Längenskala quasikristalline Strukturen erzeugt werden können. Quasikristalle sind Strukturen mit langreichweitiger Ordnung, die im physikalischen Raum nicht periodisch sind. Bisher sind fast alle quasicrystalline Strukturen, die numerisch konstruiert wurden, auf 2-dimensionale physikalische Räume beschränkt.

In dieser Arbeit wird das Phasenfeldkristallmodell für Quasikristalle auf 3-dimensionale physikalische Räume erweitert. Desweiteren wird ein grober Überblick über das Phasendiagramm des erweiterten Phasenfeldkristallmodells in drei Dimensionen gegeben. Unter den vielen verschiedenen stabilen und metastabilen Phasen in drei Dimensionen sind zwei Phasen mit gestapelten 2-dimensionalen Quasikristallen. Darüber hinaus wird gezeigt, dass verschiedene Methoden, die erfolgreich in 2-dimensionalen Simulationen angewendet werden, nicht ausreichend sind, um in drei Dimensionen stabile Quasikristalle mit ikosaedrischer Symmetrie zu erzeugen.

Contents

Chapter 1

Introduction to Quasicrystals

1.1 Crystallography and fivefold symmetry

For many decades it was believed that crystals have to be periodic. Periodic crystals are constructed on a lattice. A lattice is an infinite array of points such that when translating the crystal from one point on the lattice to another, it remains invariant. The requirement for a periodic crystal to have such a lattice limits the number of rotational symmetries it can possess. It can be shown that such a periodic lattice can only have 2, 3, 4 and 6-fold rotational symmetry. A periodic lattice with 5-fold symmetry does not exist. The reason can be seen in figure 1.1.

A related problem can also be formulated in terms of tilings: Is it possible to fill a two dimensional surface with congruent tiles, such that no space is left unoccupied? This is possible for example with hexagons, but not with pentagons.

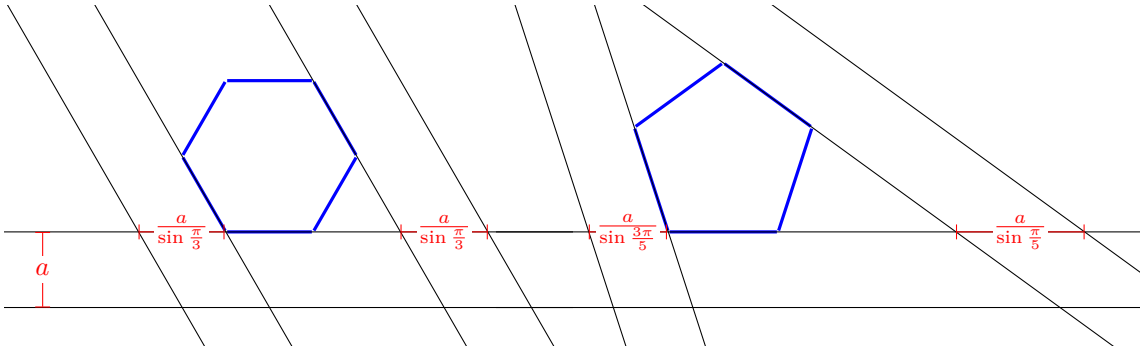

Figure 1.1: Periodically spaced lines with a distance of a parallel to the edges of a hexagon (left) and a pentagon (right). For the hexagon, the distance $a/\sin\frac{\pi}{3}$ between the intersections of the lines is the same for each of the two pairs of lines drawn. This demonstrates that it is possible to construct a periodic lattice with sixfold rotational symmetry. In case of the pentagon, the two pairs of lines have different, incommensurate distances of $a/\sin\frac{3\pi}{5}$ and $a/\sin\frac{\pi}{5}$. Therefore it is not possible to construct a periodic tiling with fivefold rotational symmetry.

The group of transformations under which a three dimensional periodic crystal can be invariant is given by the 230 crystallographic space groups [16] that have been found independently by Fedorov, Schoenflies and Barlow in the 1870s [17]. Before quasicrystals were discovered, this was seen sufficient to describe all crystals that can occur in nature.

Already before the discovery of quasicrystals, various people examined structures, where the condition to have only one unit-cell that is repeated at all lattice points is relaxed. Allowing for

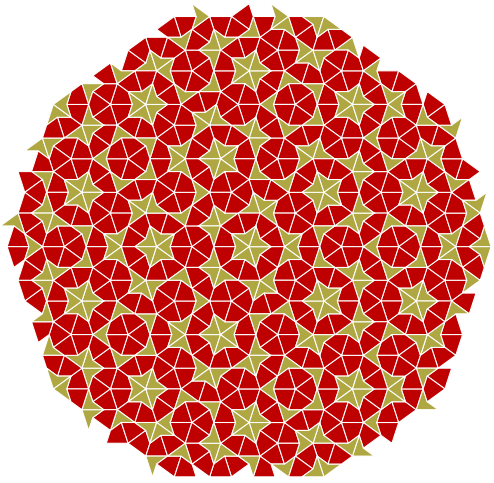

Figure 1.2: Penrose tiling constructed with two shapes “darts” and “kites”.

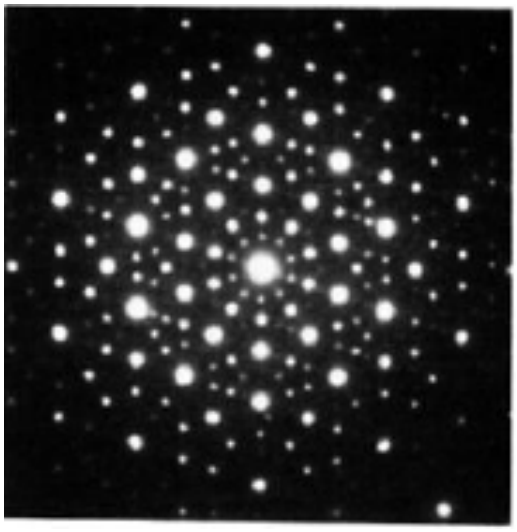

Figure 1.3: Electron diffracion pattern of Al-14-at.%-Mn as published by Shechtman *et al.* [25] in 1984

example two differently shaped tiles, one can get Penrose tilings like the example in figure 1.2. The remarkable aspect about such a tiling is: It is built deterministically with fixed rules called “matching rules” that lead to long-range order, but the tiling never completely repeats itself and therefore is not periodic. Such a two dimensional Penrose tiling can also be generalized to three dimensions, as suggested by Ammann [17].

A common method of analyzing crystallographic structures is by firing electrons or neutrons at a sample of the crystal that is studied, and looking at the diffraction patterns. This way one can obtain an image of the structure in Fourier space, that when including additional information about the phases, in principle allows to calculate the structure in real space. The rotational symmetry of a periodic crystal in this image manifests itself in the rotational symmetry of its diffraction pattern. The rotational symmetry is obtained by counting the number of peaks in the corresponding plane. In order to match periodic crystals, the diffraction pattern cannot have 10 peaks because a fivefold rotational symmetry does not allow a periodic lattice to exist.

In 1984 Shechtman [25] published diffraction patterns of an aluminium manganese alloy that has icosahedral symmetry. The diffraction pattern of the fivefold rotation axis is depicted in figure 1.3. This lead to a new era in crystallography. The International Union of Crystallography changed its definition of the term “crystal” from periodic structures to “structures with essentially discrete diffraction patterns” to include aperiodic structures [1] and in 2011 Shechtman was awarded the Nobel prize in chemistry for his discovery.

1.2 Properties and applications of quasicrystals

Due to their unique features, quasicrystals have a wide range of possible technological applications [10]. Properties that could offer a solution to various common problems include

- low friction, nonstick properties
- low thermal conductivity
- repairing dislocation glides
- corrosion resistant surfaces
- different electric properties depending on temperature
- a complete photonic band gap for low dielectric contrasts [23, 28]

Although quasicrystals have been an active area of research for some time, basic requirements needed, if one wants to take advantage of such properties, for example the ingredients needed for growing quasicrystals from various materials in a well-defined fashion, are still poorly understood. This is especially true for soft-matter systems.

An example of a commercially available product that used special properties of quasicrystals were the “Cybernox” frying pans by Sitram [9]. However it turned out that the quasicrystalline surface responsible for the non-stick properties was susceptible to salt.

Chapter 2

Phase Field Crystal Models

Understanding the formation of micro-structures often involve computer simulations. In a lot of cases molecular dynamics (MD) simulations are used. With present-day computers, these are severely limited in the number of particles, times and lengthscales they can handle [18]. Phase field crystal (PFC) models constitute a computationally efficient alternative to study crystal structures and their dynamics [12]. They employ a coarse-grained free-energy expansion with respect to a scalar field ψ also called *order parameter*, which can be associated with a density. Using several approximations, the scalar field ψ can be derived from density functional theory (DFT) as a non-equilibrium ensemble average of the number density.

2.1 Swift-Hohenberg equation

One of the simplest possibilities to construct a differential equation to study pattern formation has been derived by Swift and Hohenberg [27]:

$$\partial_t \psi(\mathbf{r}) = \left(\varepsilon - \left(\nabla^2 + k_0^2\right)^2\right) \psi(\mathbf{r}) - R(\psi(\mathbf{r})). \tag{2.1}$$

The time evolution of the system is determined by two parameters ε and k_0 and a non-linear function R that satisfies $R(0) = 0$. The parameter ε has the role of temperature, k_0 is a characteristic lengthscale of the system.

Finding stationary solutions of the Swift-Hohenberg equation (2.1) is convenient in Fourier space because ∇^2 transforms to $-k^2$, where k is the magnitude of the wave vector. The validity of the replacement of ∇^2 with $-k^2$ can be derived directly from the definition of the Fourier transform $\mathcal{F}$ and its inverse

$$(\mathcal{F}f)(\mathbf{k}) = \int \mathrm{d}\mathbf{r}\ f(\mathbf{r}) e^{-\mathrm{i}\mathbf{k}\mathbf{r}} \tag{2.2}$$

$$f(\mathbf{r}) = \frac{1}{2\pi} \int \mathrm{d}\mathbf{k}\ (\mathcal{F}f)(\mathbf{k}) e^{\mathrm{i}\mathbf{k}\mathbf{r}}. \tag{2.3}$$

For any integrabel function f that vanishes at $\mathbf{r} \to \pm\infty$ this means

$$\begin{aligned}(\mathcal{F}\nabla f)(\mathbf{k}) &= \int \mathrm{d}\mathbf{r}\ (\nabla f)(\mathbf{r}) e^{-\mathrm{i}\mathbf{k}\mathbf{r}} \\ &= f(\mathbf{r}) e^{-\mathrm{i}\mathbf{k}\mathbf{r}}\big|_{-\infty}^{\infty} - \int \mathrm{d}\mathbf{r}\ f(\mathbf{r}) \nabla \left(e^{-\mathrm{i}\mathbf{k}\mathbf{r}}\right) \\ &= \mathrm{i}\mathbf{k} \int \mathrm{d}\mathbf{r}\ f(\mathbf{r}) e^{-\mathrm{i}\mathbf{k}\mathbf{r}} = \mathrm{i}\mathbf{k}(\mathcal{F}f)(\mathbf{k}). \end{aligned} \tag{2.4}$$

With this, the Swift-Hohenberg equation (2.1) in Fourier space becomes

$$\partial_t \psi(\mathbf{k}) = \left(\varepsilon - \left(-\mathbf{k}^2 + k_0^2\right)^2\right) \psi(\mathbf{k}) - R(\psi(\mathbf{k})). \tag{2.5}$$

For any stationary solution given by $\partial_t \psi(\mathbf{k}) = 0$, also the right hand side of (2.5) is equal to zero. If the function R is always positive, the only solution for a temperature parameter $\varepsilon < 0$ is the constant phase $\psi = 0$, such that there is no pattern formation. The constant phase is also referred to as *liquid* or *fluid*. In the following, the investigation will focus on the non trivial cases with $\varepsilon > 0$ or $R < 0$.

2.2 Dynamical Phase Field Crystal Model

The Swift-Hohenberg equation 2.1 can be written in terms of a gradient of a scalar field F. As shown in [13], such a scalar field that depends on ψ is the local Helmholtz free energy, which will be referred to by its shorter name *free energy*. Formulated as a variation of F, the Swift-Hohenberg equation becomes an equation of the form

$$\partial_t \psi = -\frac{\delta F[\psi]}{\delta \psi}. \tag{2.6}$$

Considering for example equation 2.1 with non-linear term $R = \psi^3$, a possible potential is

$$F[\psi(\mathbf{r})] = \left(\frac{1}{2}\psi(\mathbf{r}) \left(-\varepsilon + \left(\nabla^2 + k_0^2\right)^2\right)\right) \psi(\mathbf{r}) + \frac{1}{4}\psi^4(\mathbf{r}). \tag{2.7}$$

The reason for the choice of $R = \psi^3$ will be further explained in section 2.3.2. The density field ψ evolves towards a local minimum, however in general, the mean value

$$\bar{\psi} = \int \mathrm{d}\mathbf{r}\ \psi(\mathbf{r}) \tag{2.8}$$

is going to change as well. This type of minimization of the potential is therefore called *unconserved*.

The equation 2.6 for unconserved dynamics can be replaced by a diffusion equation

$$\partial_t \psi = \nabla^2 \frac{\delta F[\psi]}{\delta \psi}. \tag{2.9}$$

This type of time evolution conserves the mean density $\bar{\psi}$ and will therefore be called *conserved*. Furthermore, the dynamics given by this equation is the same as in an over-damped physical system, allowing for example to study the growth of crystals. In the following, time will be measured in dimensionless units, derived by setting the diffusion constant to one.

2.3 Free energy functional

2.3.1 Landau theory approach

The Ginzburg-Landau theory was the first theory to phenomenologically describe superconduction. It has a classical equivalent that can be used to describe phase transitions in thermodynamic systems [19]. To describe a phase transition, it relies on an order parameter field ψ that has to be sufficiently smooth at the phase transition. Such a phase transition is for example the second-order phase transition between a paramagnetic and ferromagnetic phase which takes place at a critical temperature T_c. The order parameter ψ is the magnetization of the material, a measure for the alignment of magnetic dipoles. It is zero for temperatures T larger than the critical temperature T_c.

To describe this transition, a thermodynamic potential like the free energy $F(T, \psi)$ is used, which depends in this case on the temperature T and the magnetization ψ. The free energy F is assumed to be analytic at the phase transition and can be expanded in a Taylor series

$$F = \sum_{i=0}^{\infty} \alpha_i \psi^i \tag{2.10}$$

with coefficients $\alpha_i(T)$ that are functions of the temperature T. The Taylor expansion is then truncated at a certain order. Often terms up to fourth order in ψ are kept. The forth order ensures that the free energy F can have up to two stable equilibrium points and goes to infinity for $\psi \to \pm\infty$.

The number of coefficients $\{\alpha_0, \alpha_2, \alpha_3, \alpha_4\}$ which are left is then further reduced by symmetry considerations. For example if $\psi \to -\psi$ is a symmetry of the system, all α_n where n is odd have to vanish.

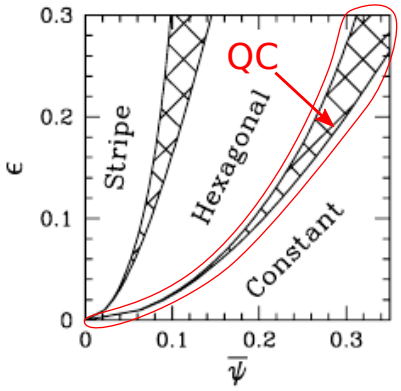

Figure 2.1: Phase diagram by K. R. Elder *et al.* [12] for a two dimensional phase field crystal model with one lengthscale. The coexistence regions are marked by the cross-hatched area. When extending the free energy to two lengthscales as in section 2.3.3, quasicrystals can be found as an additional phase in the coexistence region between the hexagonal and the constant phase marked in red.

2.3.2 Interaction potential with one lengthscale

In Landau's theory, the phase obtained after minimization depends on the lowest order terms in the expansion of the free energy F in equation 2.10. The first order term, linear in ψ, can be neglected because integrals over terms linear in ψ are constant [13].

Hence, the lowest contributing term is of second order. Any local free energy $F(k)$ has to have a minimum for a value $k > 0$, such that a non constant crystal structure with $k > 0$ can be stable. A free energy like (2.7), written in Fourier space as

$$F[\psi(k)] = \frac{1}{2}\psi\left(-\varepsilon + \left(k_0^2 - k^2\right)^2\right)\psi + \frac{1}{4}\psi^4 \tag{2.11}$$

satisfies this requirement: It has a minimum at a value $k = k_0$. In addition, the free energy needs a term that can lower the energy of an ordered phase below the energy of a liquid. In the model (2.11)

this is done by choosing $\varepsilon > 0$. Finally, the fourth order term needed to ensure that $F \to \infty$ for $k \to \pm\infty$ for any value of ε.

The structure obtained by minimizing the free energy functional like (2.7) with one lengthscale k_0, depends on the two remaining parameters. This is the temperature parameter ε and the mean density $\bar{\psi}$ which can be varied.

In two dimensions and for one lengthscale there are two different ordered phases and the constant phase that can be observed to have the lowest free energy. Each phase occurs in its own region in the phase diagram in figure 2.1. Between different phases there is a coexistence region. At $(\bar{\psi} = 0, \varepsilon = 0)$ there is a triple point where all phases coexist. The two ordered phases are the stripe phase which occurs at lower densities and the hexagonal phase which occurs at medium densities. For the stripe phase (figure 4.1 (a)), the separation of two stripes is equal to $2\pi/k_0$. For the hexagonal phase (figure 4.1 (h)), $2\pi/k_0$ is the edge length of a triangle.

2.3.3 Interaction potential with different lengthscales

The free energy (2.11) can be modified to model particles an interaction potential with several lengthscales k_i, each lengthscale being a minimum of the free energy

$$F[\psi(k)] = \frac{1}{2}\psi\left(-\varepsilon + \prod_i \left(k_i^2 - k^2\right)^2\right)\psi + \frac{1}{4}\psi^4. \tag{2.12}$$

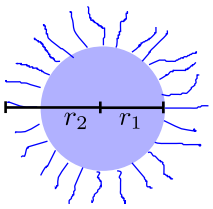

Figure 2.2: Scematic drawing of a colloid with two incommensurate radii r_1 and r_2.

In practice, such a system is for example consisting of attracting spherical particles with a hard core and a soft edge. Ihe interaction potential then has two minima for the two different radii. If two incommensurate lengthscales are selected, it is possible to obtain quasicrystals [24, 2].

For two dimensional quasicrystals with tenfold symmetry, the lengthscales of the wave-vectors in Fourier space are $k_0 = 1$ and $k_1 = 2\cos\frac{\pi}{5}$, such that the ratio is $\frac{k_1}{k_0} = \tau$ which is the *golden ratio*. The name golden ratio refers to the fact that a rectangle constructed with such a ratio is believed to be most aesthetically pleasing [11]. The ratio also has certain special properties, like $\tau + 1 = \tau^2$.

The free energy for these two lengthscales becomes

$$F[\psi(k)] = \frac{1}{2}\psi\left(-\varepsilon + \left(1 - k^2\right)^2\left(\tau - k^2\right)^2\right)\psi + \frac{1}{4}\psi^4. \tag{2.13}$$

In equation 2.13, the minima of the two lengthscales k_0 and k_1 have the same energy. At least one of the two minima has to be to be below zero, ensuring that the ordered phase can have a higher energy than the liquid. This can be done with a temperature parameter $\varepsilon > 0$ as shown in figure 2.3. If the aim is to remain inside the red marked region in the phase diagram in figure 2.1 where quasicrystals can be found for two dimensional systems with two lengthscales [2, 13, 24, 21], the average density $\bar{\psi}$ has to be changed accordingly when changing ε.

In those systems, the quasicrystalline phase looks different for different distances to the triple point. In two dimensional systems it has been shown that for quasicrystals close to the triple point, the height of the main Bragg peaks compared to the side peaks is significantly larger. Additionally, when looking at a “flower” in real space (i.e. one center peak surrounded by ten neighboring peaks,

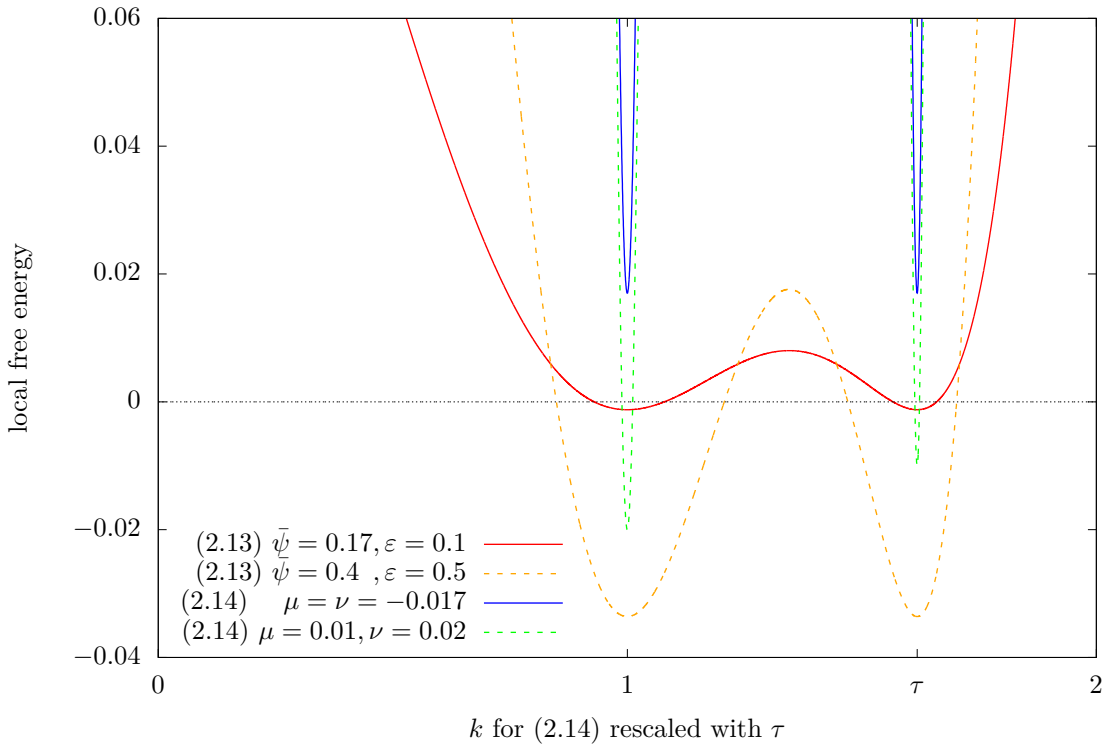

Figure 2.3: Local free energy functionals (2.13) and (2.14) as a function of the wave number k. For (2.14), parameters $Q = 1$ and $\sigma_0 = -100$ and an average value of $\bar{\psi} = 0$ for the non-linear terms were chosen to match [26]. The contributions of terms non-linear in ψ are calculated with the average value $\bar{\psi}$ instead of the actual ψ that depends on the structure, because for more realistic values of ψ, assumptions about its amplitudes are needed. Since for (2.14), $\bar{\psi} = 0$, the non-linear terms do not contribute in this plot.

or twelve for a twelve-fold quasicystal as in [2]), the surrounding peaks have similar intensities [2].

Which lengthscales have to be chosen for the model given by equation 2.12 to produce stable quasicrystals in three dimensions? The answer is not known yet. However, it is known that three-wave interactions are needed to stabilize quasicrystalline structures [4]. As motivated in section 3.2.3, it is believed that supporting the two smallest lengthscales is sufficient. In three dimensions this choice also results in a ratio of $k_1/k_0 = \tau$, but with the first lengthscale k_0 slightly larger than one.

2.3.4 Different weights for two lengthscales

Recently there has also been a study of phase field crystal models in three dimensions [26]. The free energy functional that was used differs from equation 2.13. It can be written as

$$F[\psi(k)] = -\frac{1}{2}\psi\left(\frac{k^2\left(\mu A(k) + \nu B(k)\right)}{q^4\left(1-q^2\right)^3}\frac{\sigma_0}{q^4}\left(1-k^2\right)^2\left(q^2-k^2\right)^2\right)\psi - \frac{Q}{3}\psi^3 + \frac{1}{4}\psi^4 \tag{2.14}$$

with

$$A(k) = \left(k^2\left(q^2-3\right) - 2q^2 + 4\right)\left(q^2-k^2\right)^2 q^4 \tag{2.15}$$

$$B(k) = \left(k^2\left(3q^2-1\right) + 2q^2 - 4q^4\right)\left(1-k^2\right)^2 \tag{2.16}$$

and the two lengthscales of value 1 and $q = 1/\tau$. While the general mechanism of the two lengthscales with ratio τ is the same, it has more parameters. Among those are μ and ν which allow to independently set the depth of the two minima at $k = 1$ and $k = q$ respectively, the factor σ_0 that controls the sharpness of the peaks and the factor Q that allows to tune the interaction strength of the nonlinear interactions in the ψ^3 term. In [26], the values were chosen as $\sigma_0 = -100$ and $Q = 1$.

In contrast to the model (2.14), the free energy (2.13) which was mainly used in this study, does not have a third order term in ψ. Instead, the average density $\bar{\psi}$ is used as a parameter. When substituting ψ with $(\psi - \bar{\psi})$ in equation 2.13 and collecting the terms for each order in ψ we get

$$F[\psi(k) - \bar{\psi}] = \frac{1}{2}\left(-\varepsilon + L + \frac{1}{2}\bar{\psi}^2\right) + \left(-\varepsilon + L - \bar{\psi}^2\right)\bar{\psi}\,\psi + \frac{1}{2}\left(-\varepsilon + L + 3\bar{\psi}^2\right)\psi^2 - \bar{\psi}\,\psi^2 + \frac{1}{4}\psi^4 \tag{2.17}$$

with L the linear term

$$L = \left(1 - k^2\right)^2\left(\tau - k^2\right)^2. \tag{2.18}$$

The ψ^3-term in (2.14) can be recovered by replacing the parameter $\bar{\psi} = \frac{1}{3}Q$. According to [26], icosahedral quasicrystals are stable when choosing $\mu = \nu$ and small negative values for both of them. With this, the minima for the linear term are above zero as shown in the blue curve in figure 2.3. This is possible, because for values of $-\mu = -\nu$ on the order of $-\mu = 0.017$, the ψ^3 term can lower the energy below the liquid phase. Since $\bar{\psi} = 0$ is constant and not a parameter, the liquid phase always has an energy of $F = 0$ in this model.

Chapter 3

Numerical Methods

"Computational discovery of quasicrystals in three dimensions is much less developed [than the computational approaches in two dimensions]. Because there is no general strategy to search for quasicrystals, observations are often accidental or require trial-and-error" [8]. The following section will explain the strategies and algorithms used to overcome these challenges.

3.1 Fast Fourier Transform

To numerically compute the Fourier Transform, there are several libraries that implement Fast Fouier Transform (FFT) algorithms. After tests with the GPU-based CuFFT libraries, the CPU-based FFTW3 library [14] was chosen, because file sizes of around 8 Gigabytes for a 1024^3 array of doubles are too large for average GPU-RAMs and transferring data between CPU and GPU memory becomes time-consuming. Another advantage of the CPU based FFTW3 library is portability and the easier parallelization of CPU based code.

From the definition of the Fourier transform in equation 2.2 it can directly be seen that for a real function $f(\mathbf{r})\colon \mathbb{R}^n \to \mathbb{R}$, the Fourier transform satisfies

$$(\mathcal{F}f)(-\mathbf{k}) = (\mathcal{F}f)^*(\mathbf{k}) \tag{3.1}$$

where * denotes complex conjugation. When transforming a real density field, half of the resulting complex values are therefore just complex-conjugates which can be calculated from the other half of the values. When specifying that the input array is real, the FFTW libraries do not output values for negative k_x. The size of an $N \times M$ array becomes $\left(\lfloor \frac{N}{2} \rfloor + 1\right) \times M$ in Fourier space as shown in the example in figure 3.1. In the notation used here, the index i that runs until N refers to the x axis and the second index j that runs until M to the y axis. For the data-layout as required by the FFTW algorithms however, the $N \times M$ array would be written in row-major order as $M \times N$. In other words: When stepping through the adjacent memory locations, the index i varies most quickly.

An *in-place* transformation is more efficient and can re-use memory allocated for the real array for storing the Fourier transform. For an in-place transformation, the real array has to be padded with two additional rows or one additional row if the number of rows N is even. For an *out-of-place* transformation, no padding is required, but two arrays with different sizes have to be allocated.

For simplicity, consider a two dimensional case $\mathbf{r} = (x, y)$. The first column in the output array in

figure 3.1 corresponds to $x = 0$. For this column as well as the very last column, the constraint in equation 3.1 is also true when replacing $\mathbf{r}$ with y. For an input array that does not satisfy a required symmetry like $B_{0,1} = B^*_{0,-1}$, FFTW uses the average of the different real parts and the average of the complex and negative complex part of the two inconsistent values. For this reason it is possible to have unphysically large values in the amplitudes of these values in Fourier space. The values then compensate each other when transforming back to the array in real space [15].

When discretizing the function $f(\mathbf{r})$ in real space, the function becomes periodic in Fourier space. In the data layout, values that would have an index $j > \left\lfloor \frac{M}{2} \right\rfloor$ in Fourier space, refer to negative k_y values, such that M has to be subtracted from j for calculating k_y.

These FFTW3 transformations are unnormalized. The values have to be divided by the number $N \cdot M$ of doubles in the real space array after each forward transformation. After performing the reverse transformation without normalizing, the values are equal to the original ones.

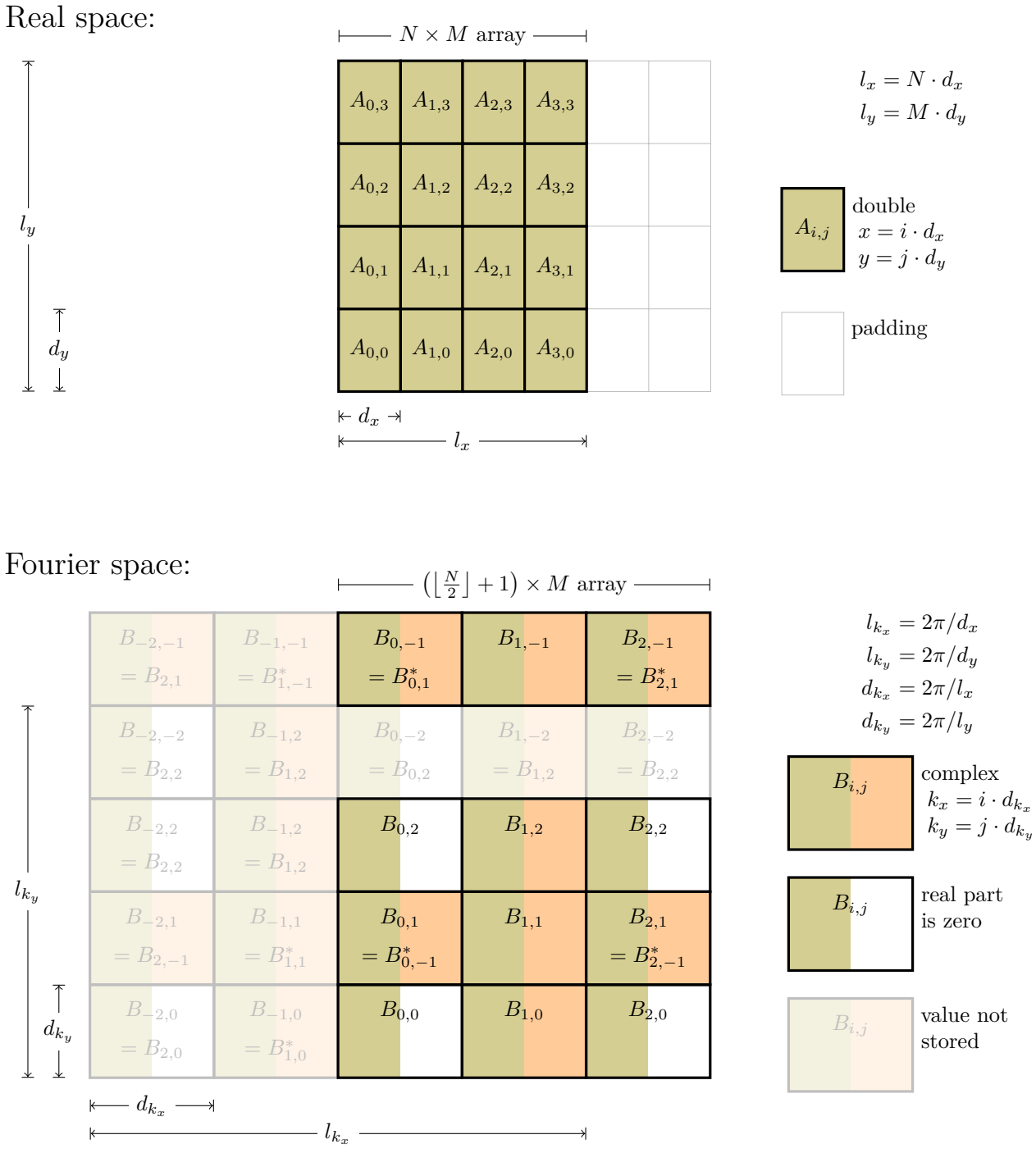

Figure 3.1: Layout of a two dimensional example 4×4 grid in real space and the corresponding 3×4 grid in Fourier space

3.2 Generating initial configurations

A time evolution like the diffusion equation 2.9 makes the system evolve towards a local minimum of F. Generally, the result depends on the initial field used as input. Testing the phase space for stable and metastable quasicrystals is done in different ways:

One approach is using random initial configurations and search the resulting phases for quasicrystals. This method successfully works in two dimensions to produce initial conditions that evolve towards two dimensional quasicrystals, both in real and Fourier space with uniformly distributed and Gaussian-shaped radom numbers. When the amplitudes of these random configurations become too large, the values in the Fourier transform become too large and produce numeric artifacts. To avoid this, the random configurations like (a) in figure 4.1, are smoothed with a box blur, i.e. a 3×3 matrix averaging over neighbouring pixels commonly used in image processing. In three dimensions, random initial configurations have the disadvantage, that the resulting crystal structure has an arbitrary orientation, making the structure determination difficult.

A different approach is using approximations of known crystal and quasicrystal structures as input. In general, if the desired phase is at least metastable, the approximation evolves towards the desired structure and the resulting free energy can be compared to other known structures. The following section explains what methods were used to approximate tenfold quasicrystalline structures.

3.2.1 Generating monomode approximations

The field ψ is a function of the position coordinate $\mathbf{r}$. It can be decomposed into its Fourier components, or density modes

$$\psi(\mathbf{r}) = \sum_j w_j e^{\mathrm{i}\mathbf{k}_j \cdot \mathbf{r}} \tag{3.2}$$

which are indexed by j, where w_j are the complex amplitudes corresponding to the value at $\mathbf{k}_j$ in Fourier space. Ordinary crystals have a finite number of peaks in Fourier space. Quasicrystals have a discrete Fourier spectrum, therefore j can also be used as an index for the main peaks.

There are some additional requirements when using Fourier components like (3.2) to construct quasicrystals. One requirement is that the resulting order parameter $\psi(\mathbf{r})$ is real at all positions $\mathbf{r}$. This means that each j component has to have a corresponding complex conjugate. Then, the exponential function in (3.2) can be replaced with a cosine function. It can also be shown [19] that the energy cannot depend on a possible phase shift since a phase shift is only a translation of the crystal.

While a quasicrystal in general has an infinite number of density modes, only the most prominent (first order diffraction peaks) are used in the approximations. Such an approximation is refered to as *monomode approximation*. A monomode approximation can be generated in Fourier space by setting the amplitudes of the desired wave-vectors $\mathbf{k}_j$, or in real space by setting $\psi(\mathbf{r})$ for each location $\mathbf{r}$ directly to $\cos(\mathbf{k}_j \cdot \mathbf{r})$. The results of both methods compared in figure 4.27 are essentially equivalent, but there are differences with respect to the numerical precision that is possible.

A common way of describing the structure of quasicrystals is using higher dimensional spaces. The structure of an icosahedral quasicrystal, aperiodic in real space, can be constructed from a periodic crystal in a six dimensional hyperspace by choosing an appropriate cut and acceptance region [19]. The additional degrees of freedom of shifting the hyperspace perpendicular to this cut,

called *phasons*, which are not present in ordinary crystals, are the underlying reason for a lot of properties mentioned in section 1.2. For the same reason, the icosahedral basis vectors in table 3.1 can be constructed as projections of these six dimensional basis vectors. Since the phase field crystal model itself does not benefit from any features in hyperspace, the following construction of the monomode approximations are described in physical space.

3.2.2 Basis vectors in two dimensions

To generate a quasicrystalline pattern in two dimensions, five basis vectors pointing to vertices of a regular pentagon and their complex conjugates can be used. Of the five vectors, one can be written as a linear combination of the remaining four. Adding two neighboring vectors of unit length results in a vector of length τ. To make this approximation a minimum of the free energy in equation 2.13, the appropriate lengthscales in the linear term are $k_0 = 1$ and $k_1 = \tau$.

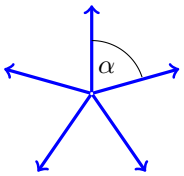

Figure 3.2: Vertex vectors for a two dimensional pentagon with angle $\alpha = \frac{2\pi}{5}$.

3.2.3 Basis vectors in three dimensions

There are several possible choices of basis vectors that can be used to obtain structures with icosahedral symmetry in three dimensions. The resulting structures are [19]:

- Simple Icosahedral Crystal (SIC, space group P235)
- Body-Centered Icosahedral Crystal (BCI, space group C235)
- Face-Centered Icosahedral Crystal (FCI, space group F235).

The simple and body-centered are considered most relevant [19]. In the following, the explanations of the monomode approximations will therefore focus on these two cases.

3.2.3.1 Simple Icosahedral monomode approximation

For the monomode approximation of a SIC, the basis vectors of length one point to the twelve edges of an icosahedron as shown in figure 3.3 and table 3.1. The first vector points upwards and the following five with numbers 2 to 6 into the five directions as in the two dimensional case in figure 3.2. However, they are tilted by an angle β. The remaining six vectors with numbers 7 to 12 are the negatives of the vectors with numbers 1 to 6 respectively. As explained in section 3.1, in Fourier space only numeric values for vectors with $k_z > 0$, which are the vectors with numbers 1 to 6 are saved.

In such a structure, the main diffraction spots occur at the positions of these 12 vectors at a distance of $|\mathbf{k}| = 1$ to the origin like shown in section 4.2.2.5. All other locations of diffraction spots are linear combinations of these vectors as shown in section 4.2.2.2, with no systematic extinctions [19]. 30 combinations of two of these vectors result in the distances $|\mathbf{k}| = 1/\sin\alpha \approx 1.052$ and another 30 combinations in a distance of $|\mathbf{k}| = \tau/\sin\alpha \approx 1.701$. These two shells, shown in section 4.2.2.10, have more vectors than the first shell with $|\mathbf{k}| = 1$. Also, the value of $1/\sin\alpha$ is very close to one. Therefore, in the free energy functional with two lengthscales (2.13), only the lengthscales

$k_0 = 1/\sin\alpha$ and $k_1 = \tau/\sin\alpha$ are supported. This requires the energy penalty for the 12 basis vectors with length one to be low enough.

3.2.3.2 Body-Centered Icosahedral monomode approximation

Both of the two shells with the thirty vectors obtained by adding two vertex vectors point to the edges of an icosahedron. These make up the basis vectors for the body-centered icosahedral phase. The distinguishing feature of the resulting quasicrystal is, that it has systematic extinction rules, that allow only linear combinations of an even number of vertex vectors in table 3.1. Furthermore in the following section, a monomode approximation with these 60 edge vectors like presented in section 4.2.2.10 differs from a monomode approximation using all $12 \cdot 12$ linear combinations of vertex vectors like presented in section 4.2.2.2 by excluding vectors with length two, generated by adding the same vertex vector twice.

The monomode approximation with edge vectors has been used as initial configuration in two varients with different orientation. One that is derived from linear combinations of the vertex vectors in table 3.1 and one is obtained by using the coordinates derived in [20] For the latter, the fivefold rotation axis is tilted by an angle of $\arcsin(\sin(\alpha)\sin(\beta))$ in the xz-plane.

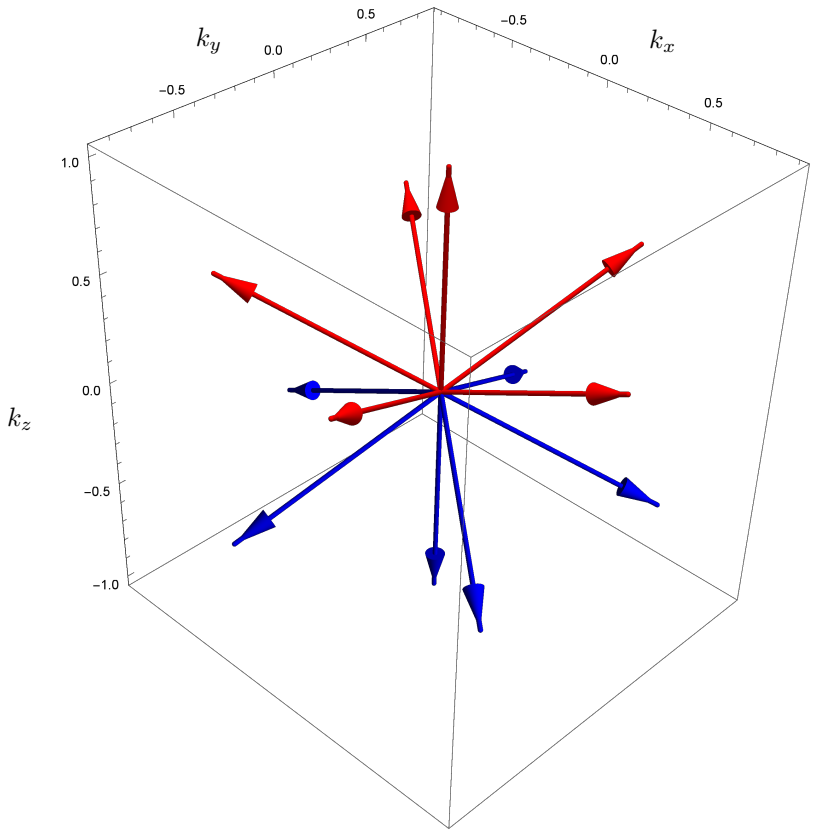

Figure 3.3: Vertex vectors of an icosahedron in three dimensional physical space that can be used as basis vectors for icosahedral quasicrystals. The vectors with positive k_z values shown in red have corresponding negative vectors shown in blue.

#	k_x		k_y		k_z	
1	0	0	0	0	1	1
2	0.2763	$\sin(\beta)\cos(\alpha)$	−0.8506	$-\sin(\beta)\sin(\alpha)$	0.4472	$\cos(\beta)$
3	−0.7236	$\sin(\beta)\cos(2\alpha)$	−0.5257	$-\sin(\beta)\sin(2\alpha)$	0.4472	$\cos(\beta)$
4	−0.7236	$\sin(\beta)\cos(2\alpha)$	0.5257	$\sin(\beta)\sin(2\alpha)$	0.4472	$\cos(\beta)$
5	0.2763	$\sin(\beta)\cos(\alpha)$	0.8506	$\sin(\beta)\sin(\alpha)$	0.4472	$\cos(\beta)$
6	0.8944	$\sin(\beta)$	0	0	0.4472	$\cos(\beta)$
7	0	0	0	0	−1	−1
8	−0.2763	$-\sin(\beta)\cos(\alpha)$	0.8506	$\sin(\beta)\sin(\alpha)$	−0.4472	$-\cos(\beta)$
9	0.7236	$-\sin(\beta)\cos(2\alpha)$	0.5257	$\sin(\beta)\sin(2\alpha)$	−0.4472	$-\cos(\beta)$
10	0.7236	$-\sin(\beta)\cos(2\alpha)$	−0.5257	$-\sin(\beta)\sin(2\alpha)$	−0.4472	$-\cos(\beta)$
11	−0.2763	$-\sin(\beta)\cos(\alpha)$	−0.8506	$-\sin(\beta)\sin(\alpha)$	−0.4472	$-\cos(\beta)$
12	−0.8944	$-\sin(\beta)$	0	0	−0.4472	$-\cos(\beta)$

Table 3.1: Coordinates in three dimensional physical space of the twelve icosahedral basis vectors shown in figure 3.3. For k_x, k_y and k_z, the right column is equal to the exact solution. In the left column, the numerical values are rounded to four significant digits. The angles are $\alpha = \frac{2\pi}{5}$ and $\beta = \arccos\left(1/\sqrt{5}\right)$.

3.3 Periodic boundary matching

A perfect quasicrystal is always infinite. A simulation or calculation can only deal with a finite number of points. The phase field crystal model also needs a finite simulation box and periodic boundary conditions as a result of the Fourier transformation. This means that the result can only be a periodic approximant of a true quasicrystal.

Since any squeezing of the crystal or sudden transition in the density leads to an increase in its free energy, the result of the minimization depends on the size of the periodic simulation box. Using the notation of the two dimensional example in figure 3.1, the size of the simulation box can be adjusted by changing the distance d_x between points in x-direction and the distance d_y between points in y-direction while keeping the volume $Nd_x \cdot Md_y$ constant.

A procedure of avoiding a strong dependence of the result on these artificial boundary conditions is by adjusting the box size after a fixed number of time-steps, minimizing the energy of the structure with respect to the boundary conditions. Even though it successfully worked in two dimensions, it adds more complexity in three dimensions. Since the goal is to obtain a quasicrystal with icosahedral symmetry, the minimization was dropped in favor of choosing a fixed size of the simulation box that favors icosahedral quasicrystals.

This is done by fitting the box to the lengths of the wave-vectors in table 3.1 in cartesian coordinates. Due to the scalar product in the exponent of (3.2), it is sufficient to look at the x, y and z direction separately. The length l that fits to wave-vector k must satisfy

$$\exp\left(\mathrm{i}\, l\, k\right) = 1, \tag{3.3}$$

such that $l\,k/2\pi$ is an integer value.

3.3.1 Lengthscales in x-direction

From the basis vectors in table 3.1 the following x-components of the wave vectors can be identified:

$$\cos\alpha\ \sin\beta, \qquad -\cos 2\alpha\ \sin\beta, \qquad \sin\beta. \tag{3.4}$$

Because all three values have a pre-factor of $\sin\beta$, the problem reduces to matching wave-vectors with length $\cos\alpha = 1/2\tau$, $-\cos 2\alpha = \tau/2$ and 1, where τ is the golden ratio. Approximating the golden ratio τ with integers is done by Fibonacci numbers f_n. The ratio of two subsequent Fibonacci numbers $f_{n+1}/f_n \approx \tau$ is the golden ratio τ. When selecting the total box-length

$$l_x = 2\pi \frac{f_n}{\cos\alpha\ \sin\beta}, \tag{3.5}$$

the values of $l_x\, k_x/2\pi$ are

$$f_n, \qquad -f_n \frac{\cos 2\alpha}{\cos\alpha} = f_n\tau^2 = f_n\tau + f_n, \qquad \frac{f_n}{\cos\alpha} = f_n 2\tau \tag{3.6}$$

for the three lengthscales in (3.4) respectively, which approach integer values for $n \to \infty$.

3.3.2 Lengthscales in y-direction

From the basis vectors in table 3.1 the following x-components of the wavevectors can be identified:

$$\sin\alpha\ \sin\beta, \qquad \sin 2\alpha\ \sin\beta. \tag{3.7}$$

Like in the previous case, excluding the $\sin\beta$ factor, the problem is reduced to finding a rational approximant for the ratio $\sin\alpha/\sin 2\alpha = \tau$. When selecting the total box-length as

$$l_y = 2\pi\frac{f_n}{\sin\alpha\ \sin\beta}, \tag{3.8}$$

the values of $l_y\, k_y/2\pi$ are

$$f_n, \qquad f_n\frac{\sin 2\alpha}{\sin\alpha} = \frac{f_n}{\tau} \tag{3.9}$$

for the three lengthscales in (3.7) respectively, which approach integer values for $n \to \infty$.

3.3.3 Lengthscales in z-direction

From the basis vectors in table 3.1 the following z-components of the wave-vectors can be identified:

$$\cos\beta, \qquad 1. \tag{3.10}$$

With $\cos\beta = 1/\sqrt{5}$, the golden ratio $\tau = \frac{1}{2}(\sqrt{5}+1)$ is rearranged to give an approximation of $\sqrt{5}$ with Fibonacci numbers:

$$\frac{\sqrt{5}}{1} = 2\tau - 1 = \frac{2f_{n+1} - f_n}{f_n} \tag{3.11}$$

The total box-length is therefore taken as

$$l_z = 2\pi\frac{f_n}{\cos\beta}. \tag{3.12}$$

3.4 Minimization methods and time evolution

One of the simplest ways to numerically compute the time evolution of dynamic systems like 2.9 and 2.6 is Euler's method. For Euler's method, the time t is discretized. For each minimization step $i = 1, 2\ldots$, the time t is increased by an amount Δt. For simplicity, the step-size Δt is taken to be constant. In an *explicit* form of Euler's algorithm, the value of ψ is changed depending on the gradient at the current time-step. The discretized equation for conserved dynamics (2.9) is then

$$\frac{\psi_{i+1} - \psi_i}{\Delta t} = \left(\nabla^2\frac{\delta F[\psi]}{\delta\psi}\right)(\psi_i) \tag{3.13}$$

such that for each time-step $i+1$

$$\psi_{i+1} = \psi_i + \Delta t\left(\nabla^2\frac{\delta F[\psi]}{\delta\psi}\right)(\psi_i). \tag{3.14}$$

The explicit method of computing the minimum becomes unstable for large values of Δt. Because $\frac{\delta F[\psi]}{\delta \psi}$ consists of a part linear in ψ, it is possible to use a *semi-implicit* algorithm where the linear term $L = -\varepsilon + (\nabla^2 - k_0^2)^2$ is evaluated at time-step $i+1$. Equation 3.13 changes to

$$\frac{\psi_{i+1} - \psi_i}{\Delta t} = \nabla^2 L \psi_{i+1} + \nabla^2 R(\psi_i) \tag{3.15}$$

and for each time-step $i+1$

$$\psi_{i+1} = \frac{\psi_i + \Delta t \, \nabla^2 R(\psi_i)}{1 - \Delta t \, \nabla^2 L}. \tag{3.16}$$

Like shown in (2.4), the factor ∇^2 can be replaced with $-\mathbf{k}^2$ in Fourier space. With $\mathcal{F}$ denoting a Fourier transform, (3.16) becomes

$$\mathcal{F}(\psi_{i+1}) = \frac{\mathcal{F}(\psi_i) - \Delta t \, \mathbf{k}^2 \mathcal{F}(R(\psi_i))}{1 + \Delta t \, \mathbf{k}^2 L} \tag{3.17}$$

with the linear term $L = -\varepsilon + (\mathbf{k}^2 - k_0^2)^2$. This time step can therefore be done in Fourier space, only the nonlinear term $R(\psi_i)$ has to be computed in real space for each step.

The results presented in chapter 4 all employ the implicit Euler equilibration (3.16). To increase stability and equilibration speed, two different possibilities were explored:

- Estimating the non-linear part with a two-step method.
- Adding small random values during equilibration.

It could be shown that both methods work, but neither of which has a significant effect on stability or equilibration speed.

Chapter 4

Results of numerical minimization

In the following chapter, results of the phase field crystal model are presented. Unless stated otherwise, all results are obtained using conserved dynamics in equation 2.9 and the semi-implicit Euler update in equation 3.16. These techniques were most easy and efficient in practice and therefore used in the majority of calculations.

Throughout this investigation, a huge number of different metastable phases were encountered. Since it is impossible to characterize and present all of them, only a tiny selection of the most interesting ones are shown. To limit the number of phases further, only results using the model presented in section 2.3.3, and only models with lengthscales $k_0 \approx 1.052$ and $k_1 \approx 1.701$ are presented. A lot of different phases can already be obtained in a limited range of parameters $\bar{\psi}$ and ε. While the resulting phases are different for other parameter ranges, the principle mechanisms and main results that were found are the same. For easier comparison as well as allowing the reader to have an idea of the position in phase space, results with parameters close to $\bar{\psi} = -0.17$ and $\varepsilon = 0.1$ are given precedence over similar results at different parameters.

4.1 In two dimensions

As a first step to three dimensional quasicrystals, the two dimensional phase space was studied. Two dimensional quasicrystals have several advantages compared to three dimensional ones:

- There are not as many possible metastable or stable phases.
- It is easy to plot and classify the resulting phases.
- It requires less computational effort.
- The results are already known [2, 24].

This is why two dimensional calculations are a good way to test and improve the methods used. The phases found are summarized in figure 4.1. The phases and the parameter ranges in the phase diagram are in good agreement with literature values, even for 12-fold quasicrystals as in [2].

With parameters on the order of $\varepsilon = 0.1$ and $\bar{\psi} = -0.17$, quasicrystals can be easily obtained from minimizing random configurations. In two dimensions the region is broad enough to allow for a deviation of ε and $\bar{\psi}$. Furthermore the relaxation of the structure is fast enough and the amplitudes of the phases large enough to avoid running into problems of limited numerical precision. This is

why the region was chosen as a starting point to explore the phase space in three dimensions. The phase diagram for three dimensional phases is expected to have a similar overall structure to the two dimensional case.

Because the free energy is symmetric with respect to $\psi \to -\psi$, all ordered phases in figure 4.1 also exist as inverse with the same free energy.

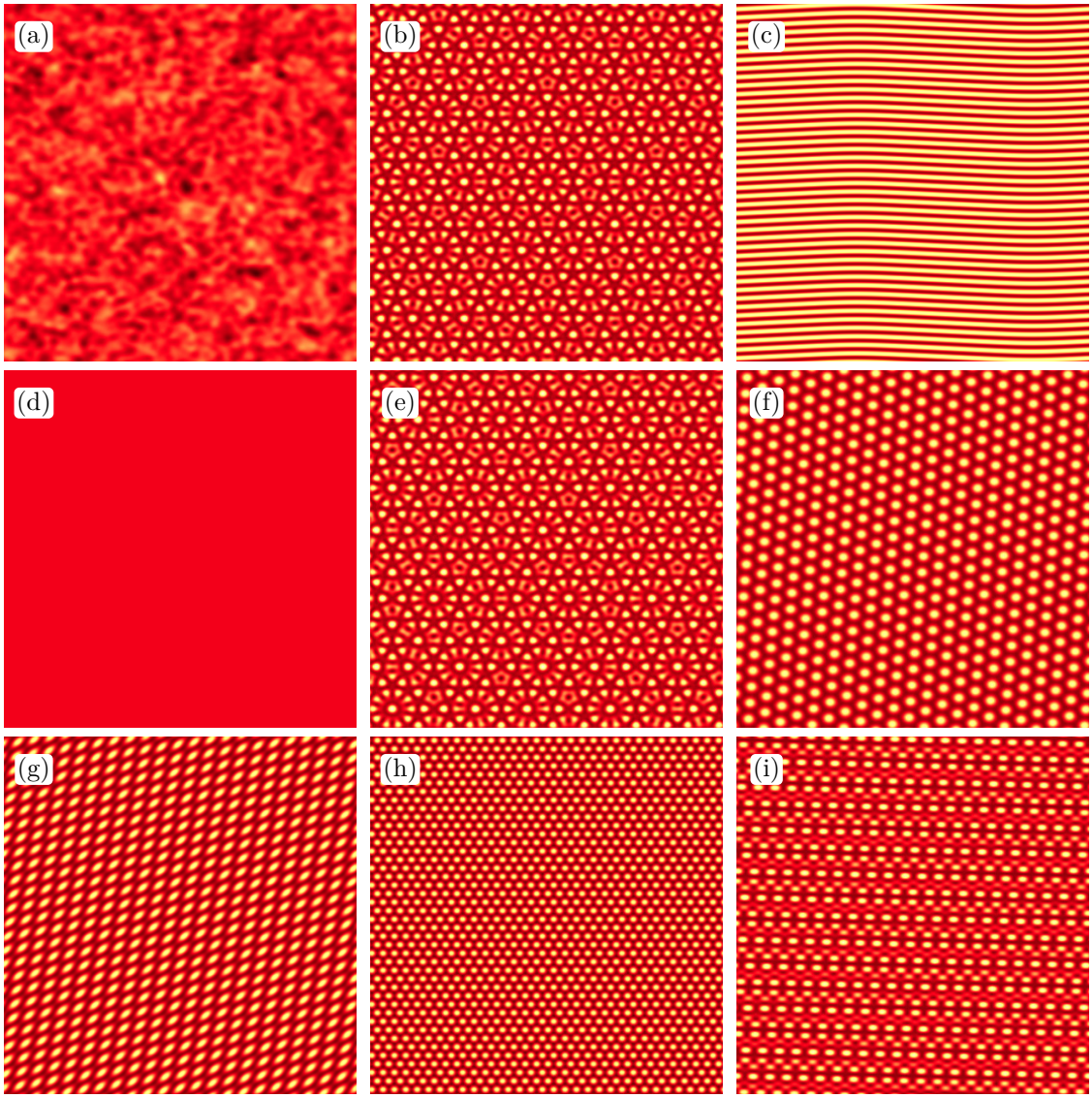

(a)	Initial random configuration	
(b)	Tenfold monomode approximation	
(c)	Stripe	(0/200)
(d)	Liquid	(0/200)
(e)	Tenfold quasicrystal	(163/200)
(f)	Large hexagonal	(2/200)
(g)	Rhombic	(11/200)
(h)	Small hexagonal	(16/200)
(i)	Archimedean tiling	(8/200)

Figure 4.1: Overview of different phases in two dimensions. In brackets the number of occurrences when minimizing 200 random configurations like (a) with mean density $\bar{\psi} = -0.17$ and temperature parameter $\varepsilon = 0.1$ is given. The phases (e)-(i) are examples of those final results while the stripe phase (c) and liquid phase (d) were obtained from minimizations with higher and lower mean density $\bar{\psi}$.

4.2 In three dimensions

Distinguishing different phases is generally easier in Fourier space. In the following chapter, peaks in Fourier space are plotted with dots. The amplitudes of the peak is proportional to the radius cubed, such that the volume of spherical dots corresponds to the amplitude of the peaks. For clarity, the zero peak that is proportional to the mean density is neglected when necessary. The peaks are colored according to their distance to the center:

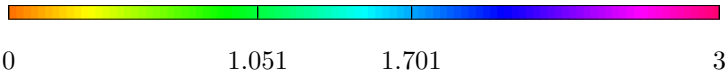

Visualizing the three dimensional data in real space is done by plotting sections in the xy-plane perpendicular to the preferred choice of the tenfold symmetry axes as well as surface plots and cuts in arbitrary directions using the visualization program VisIt [7].

4.2.1 Exploring the phase space with random initial configurations

The survey of the phase space in three dimensions was done with a box with $d_x = d_y = d_z = 0.5$, i.e. without any special adjustment of the box-length and a resolution of 128 pixel in each direction. As initial conditions, Gaussian distributed random values with a standard-deviation of 10^{-2} were chosen in real space, which were subsequently smoothed by 4 applications of a box blur image kernel.

Far from the transition to the fluid phase a lot of different phases were encountered as a result of minimization. Since icosahedral quasicrystals are expected in the region shown in figure 2.1, this investigation will focus only on a small subset of possible stable and metastable phases that are prominent close to the phase transition to the fluid phase. These are shown in figure 4.2: (a) the stripe phase, (b) the fcc phase, (c) the columnar phase.

For phases close to the liquid phase, the amplitudes of the resulting structures become small, making the determination of the resulting structure difficult. However no structure with obvious icosahedral symmetry was found. In the phase diagram in figure 4.3 these parameters are marked in red.

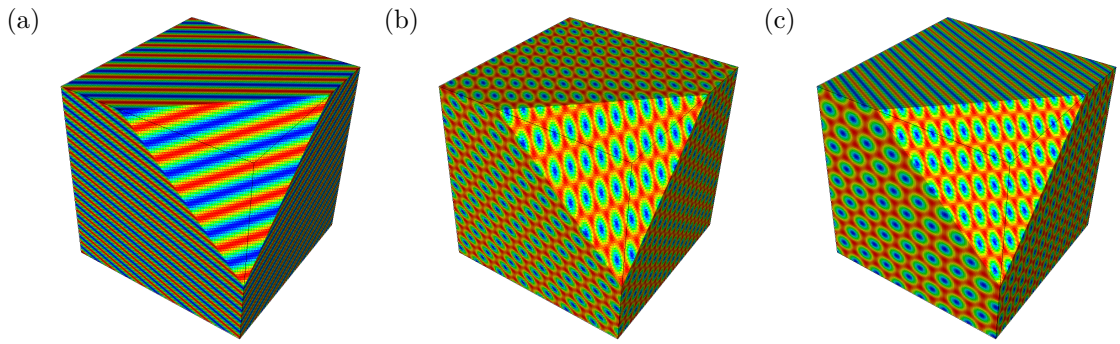

(a) Stripe phase made up of layers
(b) Hexagonal phase with FCC stacking
(c) Columnar phase with hexagonal pattern

Figure 4.2: Overview of selected phases that are present in the phase diagram in figure 4.3.

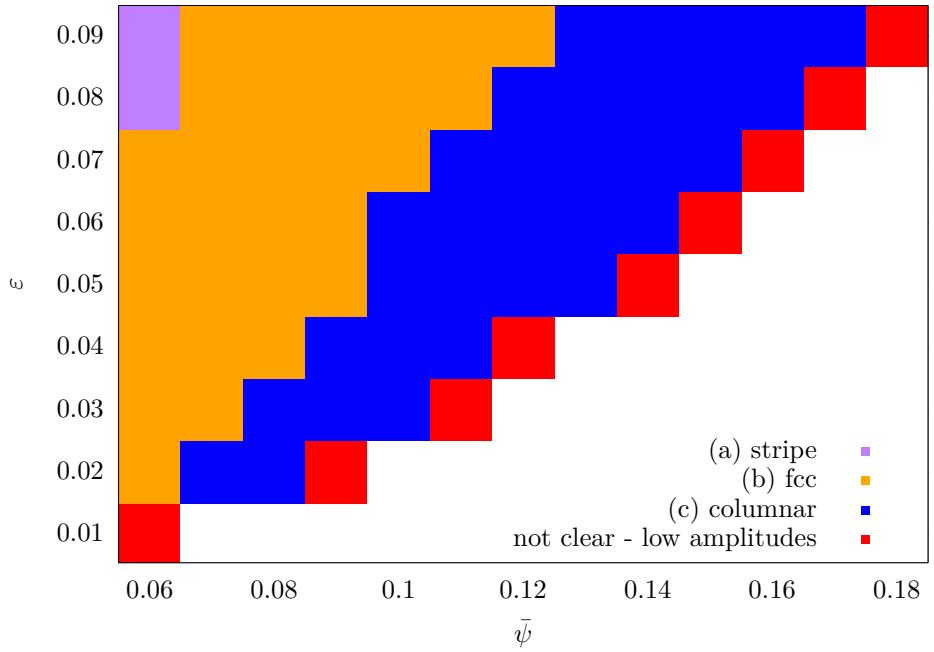

Figure 4.3: Phase diagram of resulting phases that were obtained for random initial conditions in three dimensional minimizations.

4.2.2 Energy of monomode approximations

In the following section different monomode approximations that were extracted from various results are presented. The parameters chosen as an example are again $\bar{\psi} = -0.17$ and $\varepsilon = 0.095$. They are located in the top right corner of the phase diagram in figure 4.3, in the region where columnar phases were obtained from the minimization of random initial configurations. This choice is motivated by the fact that it is far enough from the fluid phase to ensure that ordered phases like those in sections 4.2.2.1, 4.2.2.2 and 4.2.2.8 can have an energy that is lower than the fluid phase, with the energy difference still being above numerical precision limits. In addition to these practical reasons, the parameters are the same as in section 4.2.3 and similar to the two dimensional examples in section 4.1, thus the energies can be compared more easily.

The free energy is sensitive to deviations in the average density. For parameters close to the fluid phase, a small deviation of the average density and hence the free energy can already be significant. Due to limited numerical precision, the average density set with the zero component of the Fourier transform deviates by a factor of less than 10^{-14} from the average density calculated in real space and was therefore also adjusted in real space.

The monomode approximations in the following sections are sorted in decreasing order by free energy that is calculated for the above parameters. The energy is calculated for the model defined in section 2.3.3 and stated as the fraction of deviation with respect to the liquid energy F_{liq}. In this model, the liquid energy has an absolute value of around 0.1468 for the above parameters. For a random Gaussian distribution in real space with comparable amplitudes of 10^{-3}, this fraction is approximately

$$\frac{F - F_{\text{liq}}}{F_{\text{liq}}} \approx +2.$$

The size of the box was chosen as $l_x \approx 295.31$, $l_y \approx 250.98$ and $l_z \approx 295.04$ to favor quasicrystals

with the fivefold axis parallel to z and has a resolution of 1024 pixels in each direction. The approximations were done in Fourier space with the center located at the origin. The resulting energy of each approximation furthermore depends on the amplitudes, which were chosen as 10^{-5} in Fourier space. For larger amplitudes, the free energy of approximations whose energy is already lower than the fluid can be lowered further. If the amplitudes are chosen too large, the ψ^4 term in equation 2.13 becomes dominant and the ranking is different. For amplitudes on the order of 10^{-2} in Fourier space, energy differences $(F - F_{\mathrm{liq}})/F_{\mathrm{liq}}$ range from $+5.663 \cdot 10^{-4}$ for the plane wave in section 4.2.2.7 to +17.83 for the approximation in section 4.2.2.1.

For each of the monomode approximations, the first plot is a section of the xy-plane in real space at $z = 0$, and the second plot shows the three dimensional arrangement of peaks in Fourier space.

4.2.2.1 12 vertex vectors and $12 \cdot 12$ linear combinations

Of all the approximations presented here, this approximation is the one with the largest number of vectors and different lengthscales. It has wavevectors with length of approximately 1, 1.052, 1.701 and 2. There are 12 vertex vectors with lengths 1 and 12 linear combinations of the same vector that have length 2, pointing into the same direction as the vertex vectors.

For the parameters presented at the beginning of section 4.2.2, the energy ratio is

$$\frac{F-F_{\text{liq}}}{F_{\text{liq}}} = +4.190 \cdot 10^{-8},$$

larger than the fluid phase.

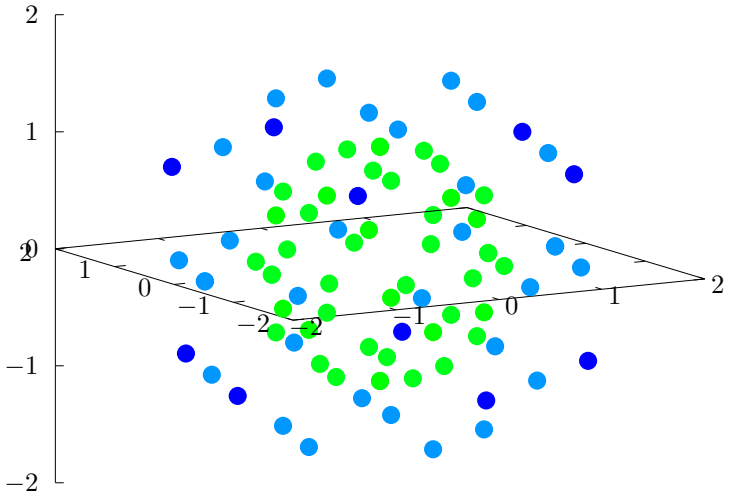

Figure 4.4: Peaks of the monomode approximation in Fourier space.

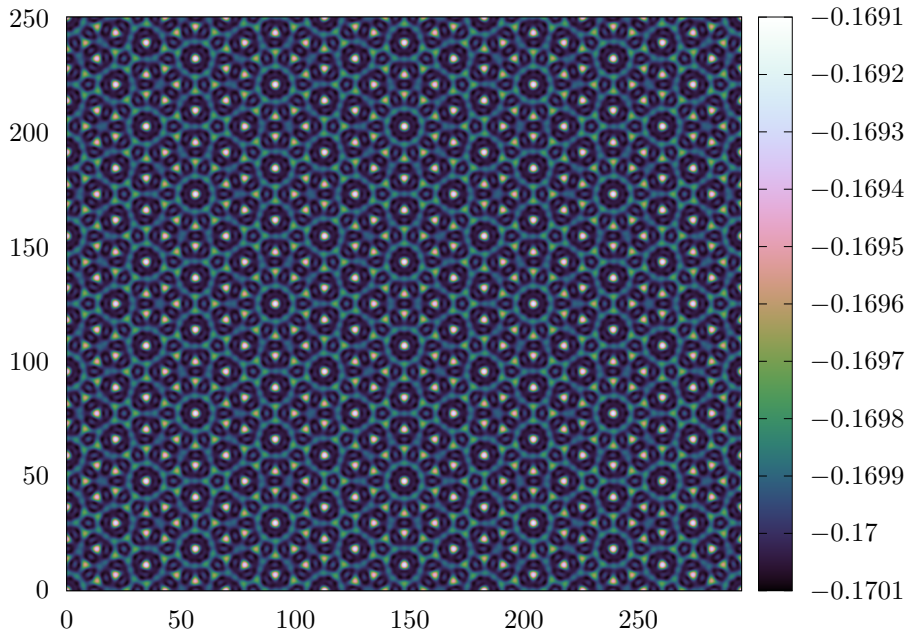

Figure 4.5: Section of the monomode approximation at the $z = 0$ plane in real space.

4.2.2.2 $12 \cdot 12$ linear combinations of vertex vectors

This approximation contains all linear combinations of vertex vectors. The wave-vectors have magnitudes of 1.052, 1.701 and 2. Compared to the approximation in section 4.2.2.1, it is missing the vertex vectors with length one.

For the parameters presented at the beginning of section 4.2.2, the energy ratio is

$$\frac{F-F_{\text{liq}}}{F_{\text{liq}}} = +4.178 \cdot 10^{-8},$$

larger than the fluid phase.

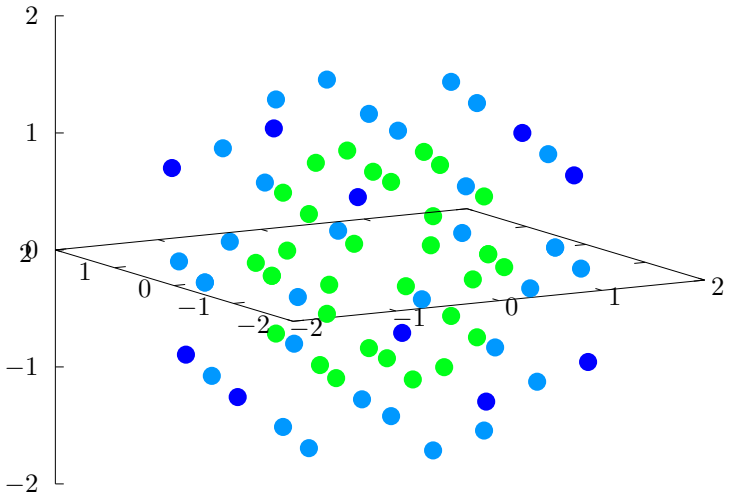

Figure 4.6: Peaks of the monomode approximation in Fourier space.

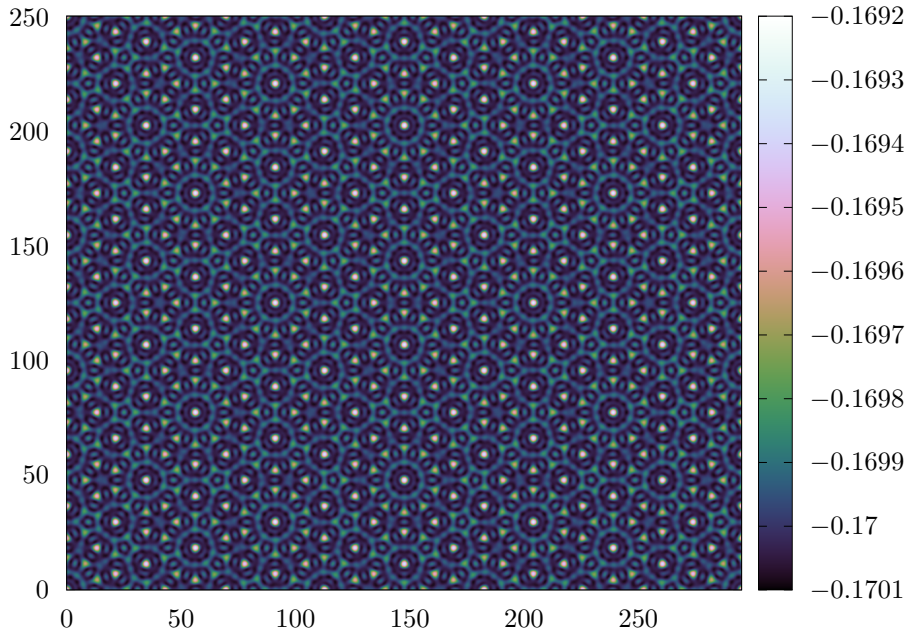

Figure 4.7: Section of the monomode approximation at the $z = 0$ plane in real space.

4.2.2.3 $10 \cdot 10$ linear combinations of vertex vectors excluding the z-direction

Compared to the approximation in the previous section 4.2.2.2, this approximation is generated from all linear combinations of two vertex vectors, but not the two vertex vectors in direction of the $+k_z$-axis or $-k_z$-axis. The approximation contains three distinct layers in z-direction which form the basis for a stacked quasicrystal in figure 4.31. Leaving out the z-direction ensures that the 5-fold symmetry with respect to the xy-plane is kept. The same approximation can be done for any direction by omitting the respective vertex vector.

For the parameters presented at the beginning of section 4.2.2, the energy ratio is

$$\frac{F-F_{\text{liq}}}{F_{\text{liq}}} = +3.474 \cdot 10^{-8},$$

larger than the fluid phase.

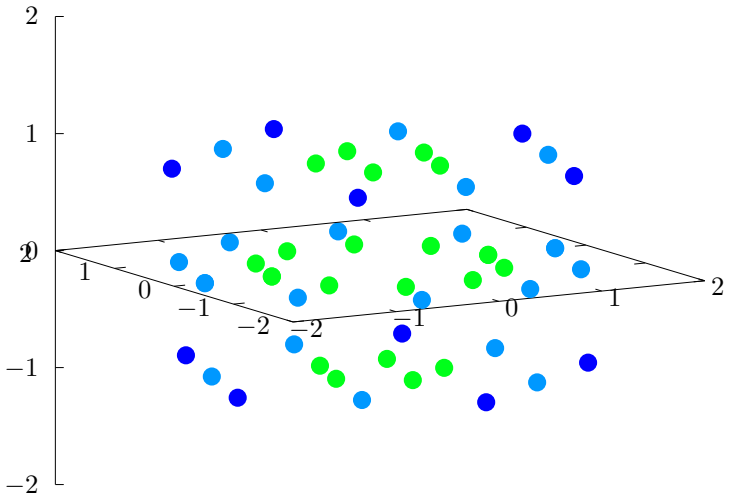

Figure 4.8: Peaks of the monomode approximation in Fourier space.

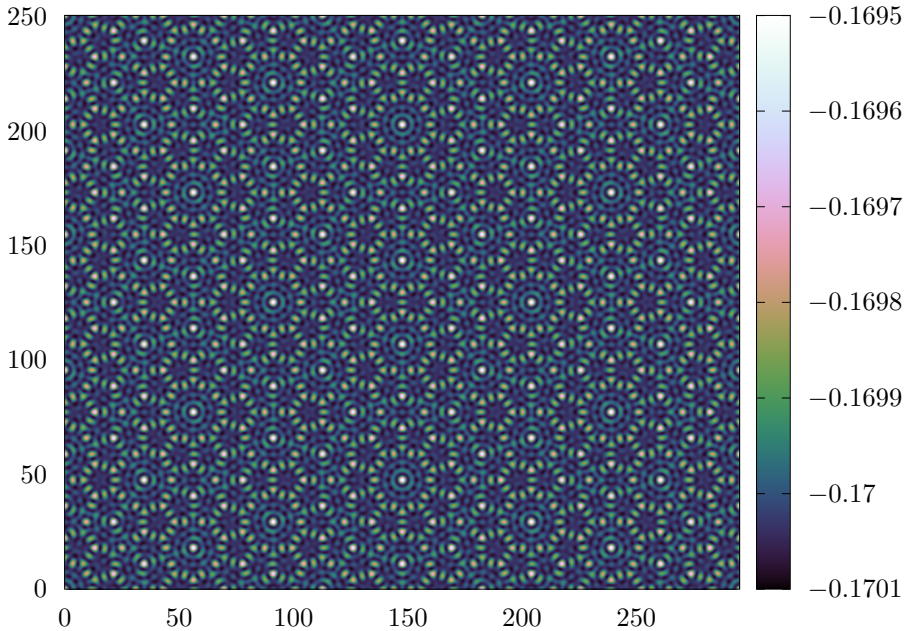

Figure 4.9: Section of the monomode approximation at the $z = 0$ plane in real space.

4.2.2.4 30 edge vectors of the first shell

The approximation uses all 30 edge vectors with length 1 in the positions specified by [20]. This orientation of the shell is inverted and tilted by an angle of $\arcsin(\sin(\alpha)\sin(\beta))$ in xz-plane and shrunk by a factor of 1/1.052 with respect to the vectors in section 4.2.2.2.

For the parameters presented at the beginning of section 4.2.2, the energy ratio is

$$\frac{F-F_{\text{liq}}}{F_{\text{liq}}} = +3.344 \cdot 10^{-10},$$

larger than the fluid phase.

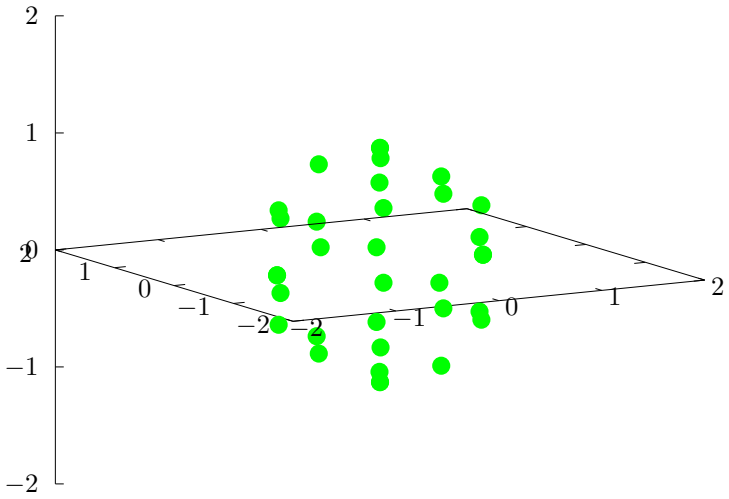

Figure 4.10: Peaks of the monomode approximation in Fourier space.

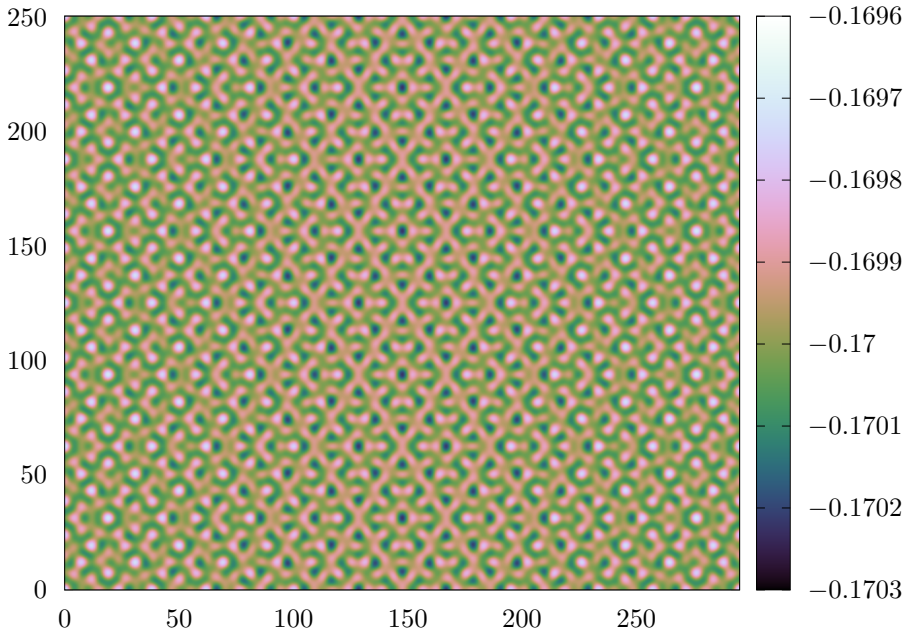

Figure 4.11: Section of the monomode approximation at the $z = 0$ plane in real space.

4.2.2.5 12 vertex vectors

The most basic approximation for icosahedral symmetry, using the 12 vertex vectors as given in table 3.1 with length 1.

For the parameters presented at the beginning of section 4.2.2, the energy ratio is

$$\frac{F-F_{\text{liq}}}{F_{\text{liq}}} = +1.286 \cdot 10^{-10},$$

larger than the fluid phase.

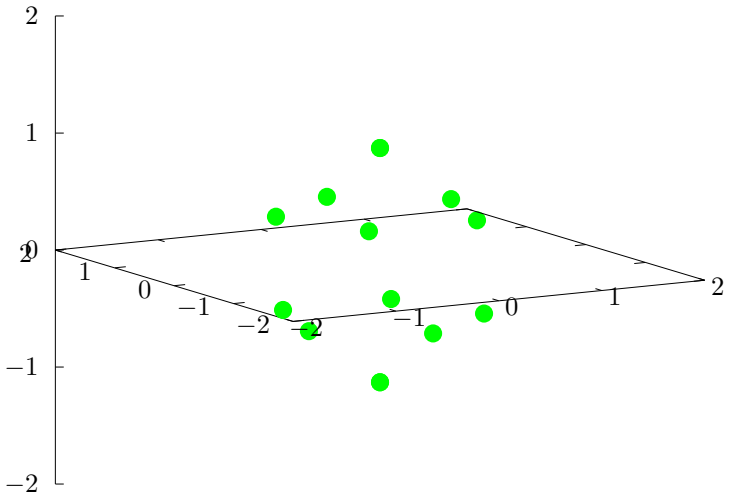

Figure 4.12: Peaks of the monomode approximation in Fourier space.

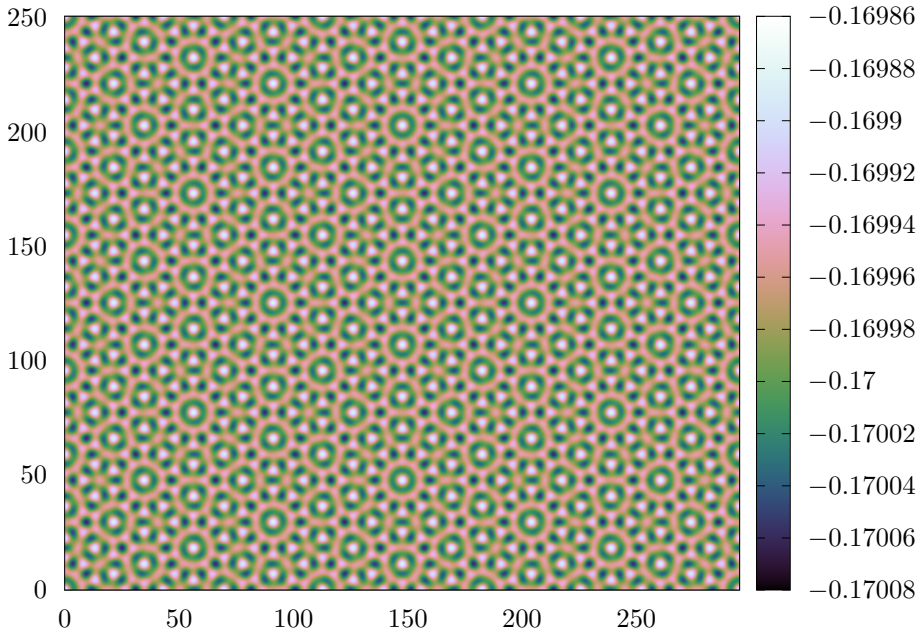

Figure 4.13: Section of the monomode approximation at the $z = 0$ plane in real space.

4.2.2.6 Cubic lattice with legthscale one

For the parameters presented at the beginning of section 4.2.2, the energy ratio is

$$\frac{F-F_{\text{liq}}}{F_{\text{liq}}} = +6.265 \cdot 10^{-11},$$

larger than the fluid phase.

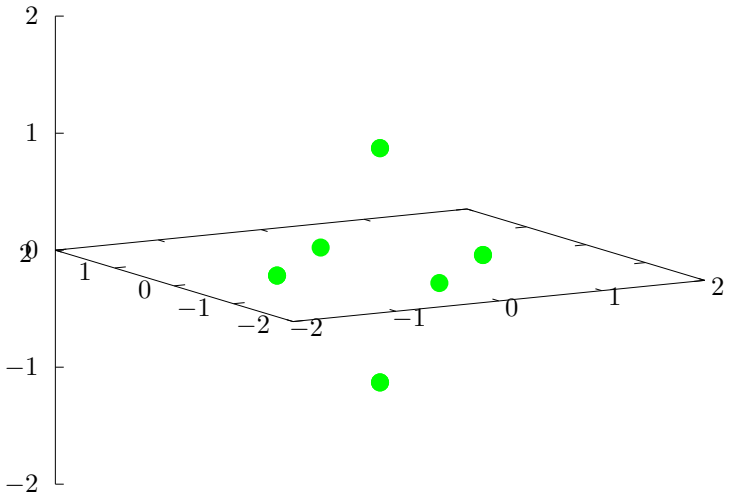

Figure 4.14: Peaks of the monomode approximation in Fourier space.

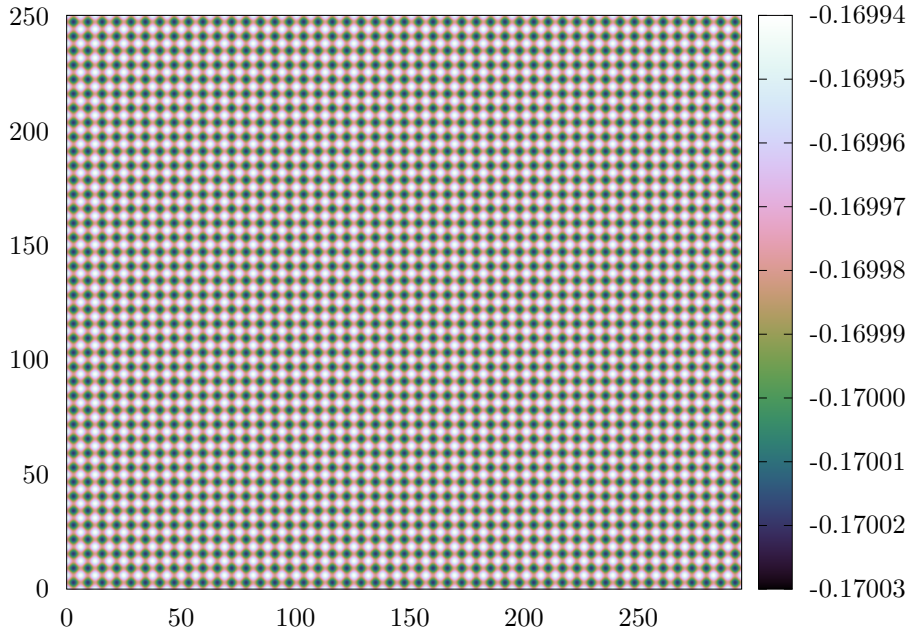

Figure 4.15: Section of the monomode approximation at the $z = 0$ plane in real space.

4.2.2.7 Plane wave with distance one in y-direction

This phase is generated by only one wave-vector with a magnitude of 1 and its corresponding negative vector. The direction is chosen parallel to the k_y axis. The result is an approximation for a stripe phase as shown in figure 4.2 (a).

For the parameters presented at the beginning of section 4.2.2, the energy ratio is

$$\frac{F-F_{\text{liq}}}{F_{\text{liq}}} = +4.824 \cdot 10^{-11},$$

larger than the fluid phase.

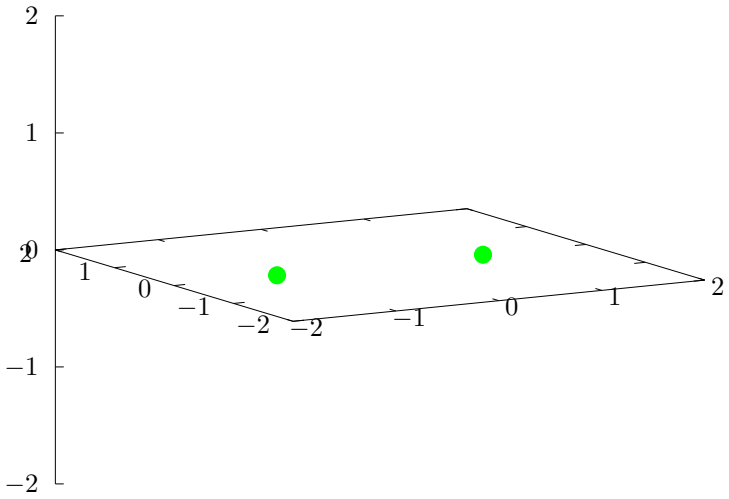

Figure 4.16: Peaks of the monomode approximation in Fourier space.

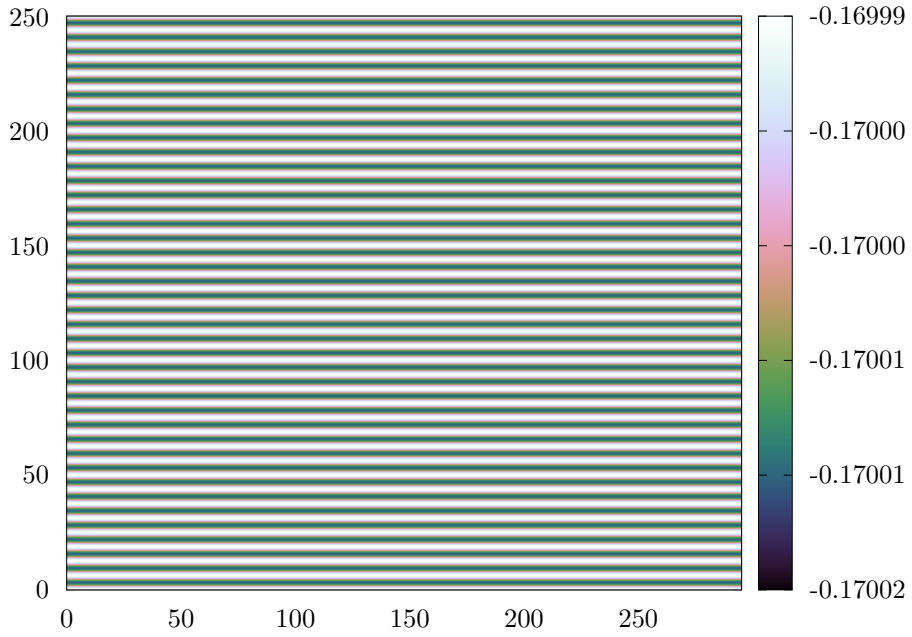

Figure 4.17: Section of the monomode approximation at the $z = 0$ plane in real space.

4.2.2.8 Selection of 14 linear combinations of vertex vectors

The selection is a rhombic phase that can be reduced to linear combinations of the vectors

$$\begin{array}{lll} (0 & , & 1.051, \quad 0 \quad) \\ (1 & , & 0.325, \quad 0 \quad) \\ (0.553, & 0 & , \quad 0.894) \end{array}$$

The phase shares all major peaks with the monomode approximation in section 4.2.2.2. For the parameters presented at the beginning of section 4.2.2, the energy ratio is

$$\frac{F - F_{\text{liq}}}{F_{\text{liq}}} = -6.810 \cdot 10^{-11},$$

lower than the fluid phase.

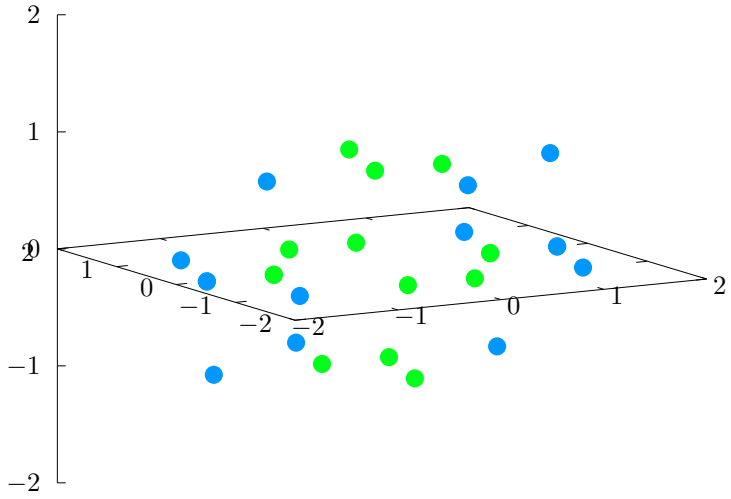

Figure 4.18: Peaks of the monomode approximation in Fourier space.

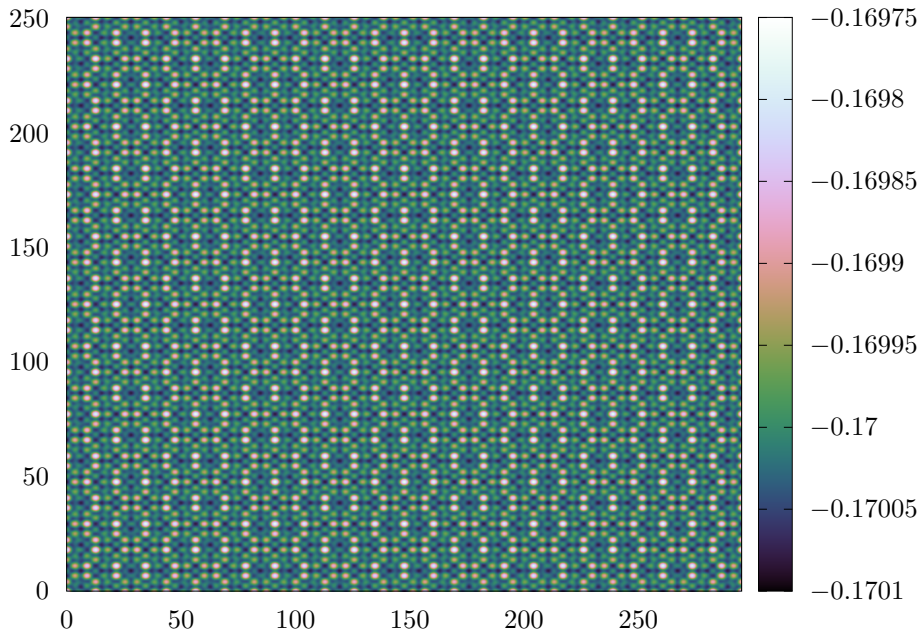

Figure 4.19: Section of the monomode approximation at the $z = 0$ plane in real space.

Metastable variants of this rhombic phase have been found as a result of several equilibrations and have a free energy between

$$\frac{F-F_{\text{liq}}}{F_{\text{liq}}} = -2.577 \cdot 10^{-3}$$

for a “dirty” variant with a lot of secondary peaks and

$$\frac{F-F_{\text{liq}}}{F_{\text{liq}}} = -3.989 \cdot 10^{-6}$$

for a “pure” variant.

4.2.2.9 60 tilted edge vectors of the first and second shell

For the parameters presented at the beginning of section 4.2.2, the energy ratio is

$$\frac{F-F_{\text{liq}}}{F_{\text{liq}}} = -1.566 \cdot 10^{-10},$$

lower than the fluid phase.

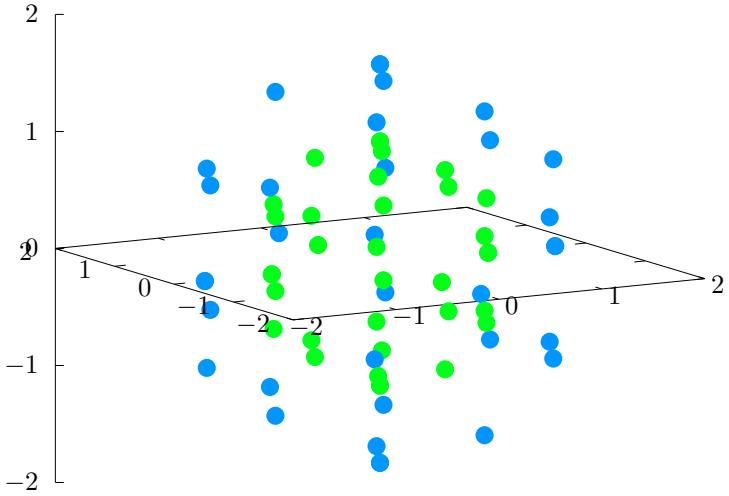

Figure 4.20: Peaks of the monomode approximation in Fourier space.

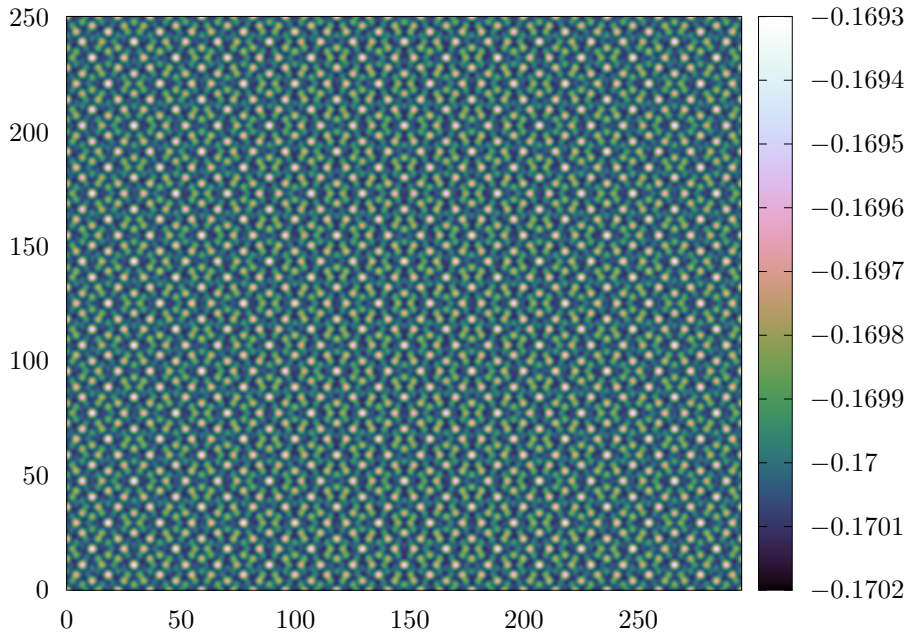

Figure 4.21: Section of the monomode approximation at the $z = 0$ plane in real space.

4.2.2.10 60 edge vectors of the first and second shell

This approximation has the lowest energy for parameters $\bar{\psi}$ and ε close to the fluid phase. The structure is the same as in the previous section 4.2.2.9, however its orientation is different. The vectors in the previous section as well as the approximation in section 4.2.2.4 have an orientation as specified in [20]. The lengthscales are 1.052 and 1.701. The same peaks are also present in the approximation in section 4.2.2.2, but the location of peaks is inverted and tilted by an angle of $\arcsin(\sin(\alpha)\sin(\beta))$ in xz-plane.

For the parameters presented at the beginning of section 4.2.2, the energy ratio is

$$\frac{F-F_{\text{liq}}}{F_{\text{liq}}} = -1.705 \cdot 10^{-10}$$

lower than the fluid phase. The simulation box supports icosahedral symmetry with an orientation of the basis as defined here, but not the orientation of the basis in the previous section 4.2.2.9. This explains the lower energy.

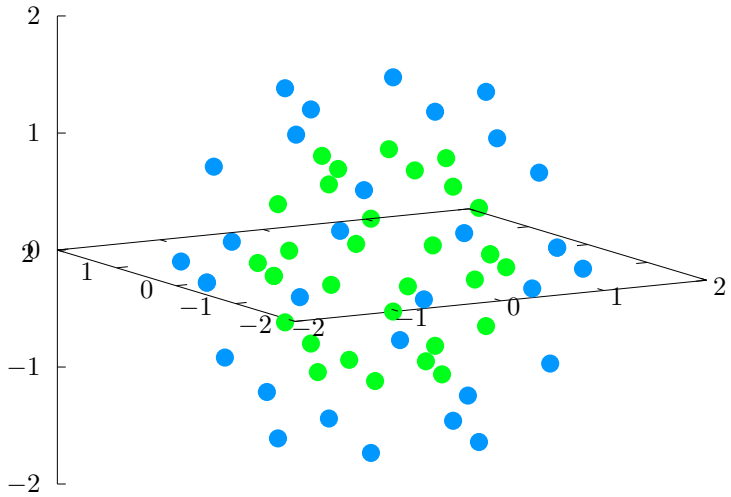

Figure 4.22: Peaks of the monomode approximation in Fourier space.

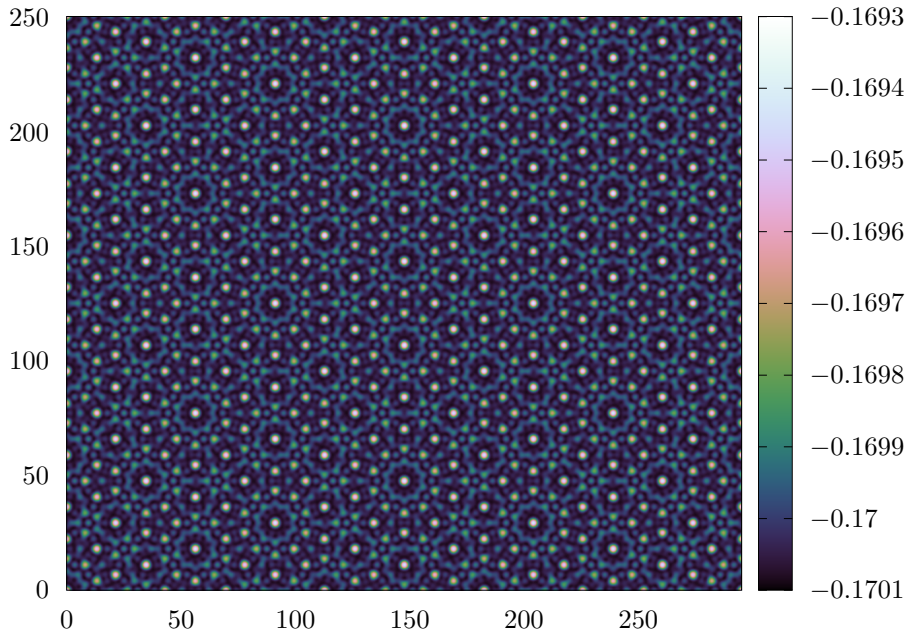

Figure 4.23: Section of the monomode approximation at the $z = 0$ plane in real space.

4.2.3 Growing two dimensional quasicrystals in three dimensions

Some methods that were tested include growing a three dimensional structure from a two dimensional input. In the presented example, a tenfold quasicrystal structure is grown in two dimensions using the same lengthscales k_0 and k_1 with a ratio of τ and parameters of $\varepsilon = 0.095$ and $\bar{\psi} = -0.17$ in both the two and three dimensional calculation. The dimensions of the box $l_x \approx 295.31$, $l_y \approx 250.98$ and $l_z \approx 295.04$ favor quasicrystals with the tenfold axis parallel to the z-direction. This is in agreement with the tenfold axis of the two dimensional input. The resolution is 1024 pixels in each direction. The tenfold quasicrystal structure is first equilibrated in two dimensions. It is then transferred to the three dimensional initial state, filling a layer at the xy-plane with a thickness of one pixel in z-direction. The remaining box is filled with a constant phase of $\bar{\psi} = -0.17$.

After 650440 iterations with $\Delta t = 1$, the change of free energy per time-step $\frac{\Delta F}{F_{\text{liq}}}$ is less than 10^{-14} and the equilibration stopped. The result is shown in figure 4.24. With

$$\frac{F - F_{\text{liq}}}{F_{\text{liq}}} = -2.189 \cdot 10^{-3},$$

the final energy is below the energy of the liquid. While sections of the structure parallel to the two dimensional input have grown a tenfold pattern that approximately matches the input, there is no clear structure apparent with respect to the z-direction. This statement is hard to prove when only looking at the real space structure in figure 4.24. But it is apparent in the Fourier space image in figure 4.25: There is an almost perfect tenfold quasicrystalline pattern in the $k_x k_y$ plane, however it appears to have irregular distances in k_z direction.

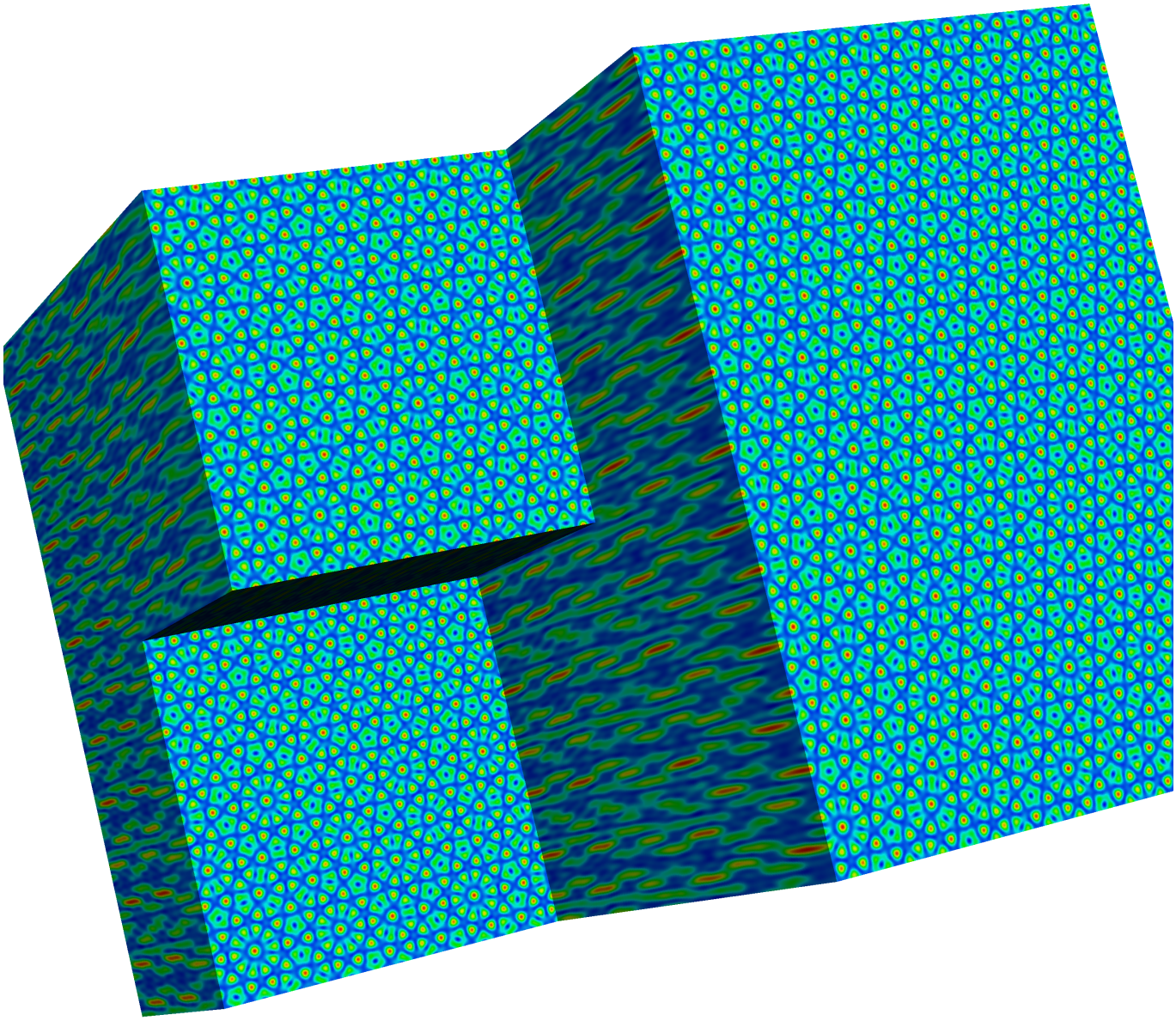

Figure 4.24: Result of growing a two dimensional quasicrystal layer after 650440 time-steps. The face shows the xy plane with cuts through the structure at three different values of z.

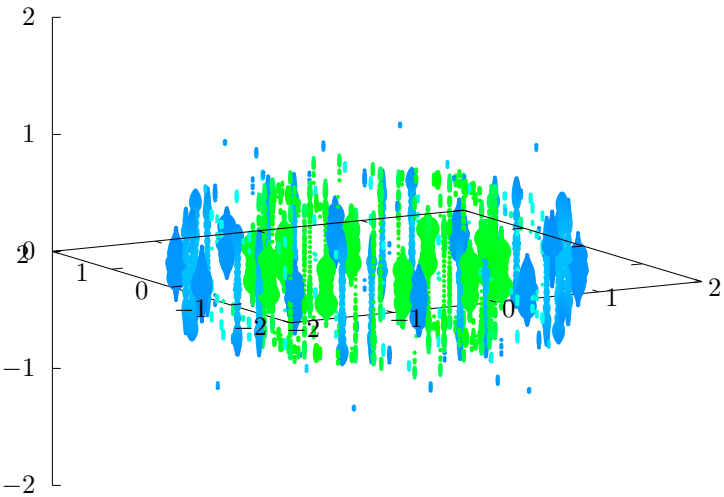

Figure 4.25: Result in figure 4.24 in Fourier space. Along the z axis that is facing upwards, the peaks do not occur in a distinct pattern.

4.2.4 Approaching the fluid phase

When looking at the phase diagram in figure 2.1, as well as the results found in the two dimensional calculations in section 4.1, stable quasicrystalline phases are expected to be found near the phase transition to the fluid phase. Therefore this region is studied in more detail.

Since the observed effects are similar for different parameters, the following results are taken from the transition at $\bar{\psi} = 0.17$ and $\varepsilon < 0.1$. The value of $\bar{\psi}$ is chosen fix and ε is varied. This has the advantage, that the same initial conditions can be chosen for each ε. Hence, small deviations of the average density and the amplitudes that could potentially have a significant effect on the resulting phase and energy do not have to be taken into account.

As a starting condition for the three dimensional calculations, the 60 edge vectors of the first and second shell, presented in section 4.2.2.10 are used. For the given parameters, this approximation has the lowest energy without additional equilibration. The amplitudes for the monomode approximation were chosen as 10^{-3}, such that for $\varepsilon = 0.088$ the starting configuration has an energy ratio of

$$\frac{F - F_{\text{liq}}}{F_{\text{liq}}} = -9.773 \cdot 10^{-7}$$

such that F is below the liquid energy. When further approaching the liquid phase, the energy of the monomode approximation becomes larger than the liquid. For $\varepsilon = 0.085$ the monomode approximation has an energy ratio of

$$\frac{F - F_{\text{liq}}}{F_{\text{liq}}} = -3.645 \cdot 10^{-7}$$

and at $\varepsilon = 0.080$ the energy ratio of the monomode approximation is

$$\frac{F - F_{\text{liq}}}{F_{\text{liq}}} = +6.624 \cdot 10^{-7}$$

above the liquid. For this value the minimization does not reach values below the fluid energy.

The equilibration was terminated when the energy change per timestep was less than 10^{-15}, which is a fraction of the total energy on the order of 10^{-14}, two orders of magnitude above the precision of approximately 10^{-16} of the double values used. The lowest energies of the phases that were obtained are plotted in figure 4.26. Except for the minimization with $\varepsilon = 0.08$ that resulted in a liquid phase, the resulting phase is roughly the same for all temperature parameters ε shown in figure 4.26. It is not an icosahedral quasicrystal, but an ordinary crystal with some modulations whose exact structure has not been further investigated.

Although it is not claimed that behavior and energies of two dimensional crystalline phases and quasicrystals are similar to their three dimensional counterparts, the energy of the quasicrystalline and hexagonal phase obtained for two dimensions with the same parameters are plotted as a reference. In the two dimensional calculations with the same parameters, it is possible to start with random initial configurations or monomode approximations with wrong parameters that have energies well above the energy of the liquid phase and still end up in the desired phase.

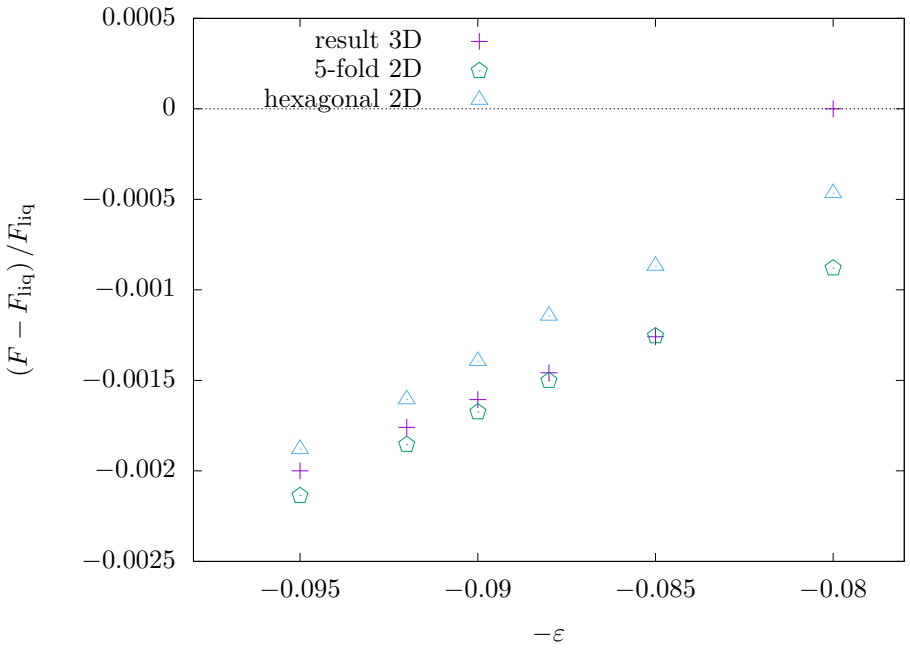

Figure 4.26: Free energy of the three dimensional crystalline phase as a function of the temperature parameter ε when approaching the fluid phase.

4.2.5 Resolution and finite size effects

There are two types of finite size effects that have to be considered:

- Finite size of simulation box and resolution of pixels in both real and Fourier space.
- Limited precision of double values.

The second point becomes relevant with decreasing distance to the fluid phase and with decreasing values of $\bar{\psi}$ and ε and thus decreasing distance to the triple point in figure 2.1. For example summing up all densities is not done by adding 1024^3 values sequentially, but by reducing the array in groups and hence minimizing rounding errors.

The finite size effects that result from a finite simulation box are coupled to the resolution in Fourier space and vice-versa by the equations stated in figure 3.1. The size of the double array used should not exceed 1024^3 double values or 8 gigabytes. Further increasing resolution in real space decreases the resolution in Fourier space. If not stated otherwise, a resolution on the order of $d_x \approx 0.2$ in real space and hence $d_{k_x} = \frac{2\pi}{1024 d_x} \approx 0.03$ in Fourier space was chosen as a compromise.

Figures 4.27, 4.28 and 4.29 show examples for finite size effects resulting from this resolution. In figure 4.27 monomode approximations generated in real and Fourier space can be compared. The size of the box was selected to fit the approximation as described in section 3.3. The artifacts become larger for monomode approximations that do not match the boundary conditions.

Figures 4.28 and 4.29 show the result of minimization of the monomode approximations in section 4.2.2.10 and 4.2.2.9 respectively. The approximation 4.2.2.10 in figure 4.28 fits into the box, while the approximation 4.2.2.9 in figure 4.29 has the same structure but is tilted and does not fit into the box. While both results are not the desired icosahedral quasicrystal, the structure 4.2.2.10 has a lower energy and less pronounced secondary peaks.

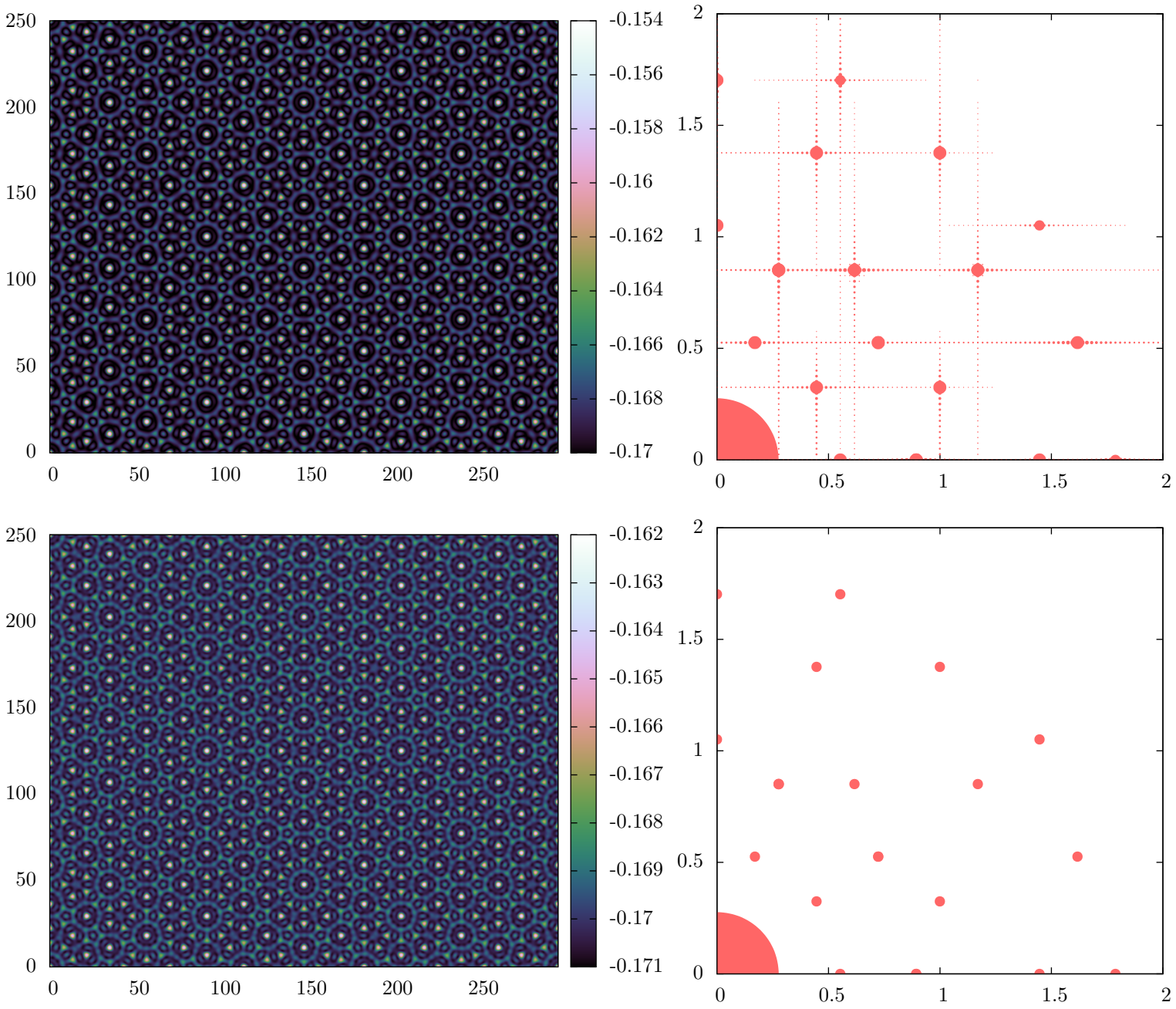

Figure 4.27: Comparison of monomode approximations generated in real space (top) and Fourier space (bottom). The left plot shows a section of the xy-plane in real space and the right a projection of the corresponding Fourier space peaks. The amplitude of the peaks correspond to the radius of the dots cubed.

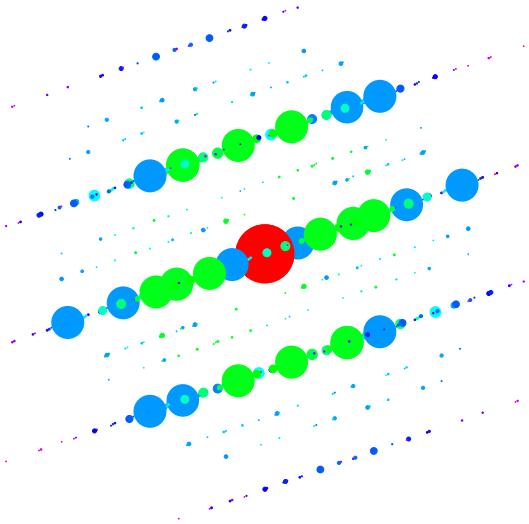

Figure 4.28: Fourier peaks of the resulting phase obtained with initial conditions fitting to the size of the simulation box.
The ratio of the free energy is $2.158 \cdot 10^{-4}$, lower than fluid phase.

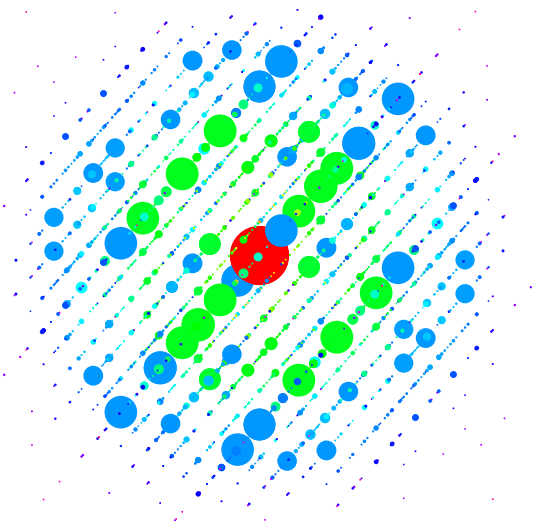

Figure 4.29: Fourier peaks of the resulting phase obtained with a rotated initial configuration.
The ratio of the free energy is $2.142 \cdot 10^{-4}$, lower than fluid phase.

4.2.6 Metastable stacked quasicrystals

Among a lot of crystalline phases, two different kinds of stacked two-dimensional quasicrystals were discovered which appear to be metastable. They can be distinguished by the distance between two stacking layers in Fourier space.

One of the two stacked quasicrystals has a separation of around 0.5 shown in figure 4.30. It occurs at parameters of $\bar{\psi} = -0.4$ and $\varepsilon = 0.5$ and is not stable in the region around $\bar{\psi} = -0.17$ and $\varepsilon = 0.095$ which is mainly discussed here. It has an absolute free energy of 0.776 193 754 or

$$\frac{F - F_{\text{liq}}}{F_{\text{liq}}} = -1.197 \cdot 10^{-2},$$

lower than the fluid phase.

The stacked quasicrystal with a separation of around 0.8 shown in figure 4.31 appears to be metastable at $\bar{\psi} = -0.17$ and $\varepsilon = 0.095$ and has an absolute free energy of 0.146 501 919 or

$$\frac{F - F_{\text{liq}}}{F_{\text{liq}}} = -1.843 \cdot 10^{-3},$$

lower than the fluid phase.

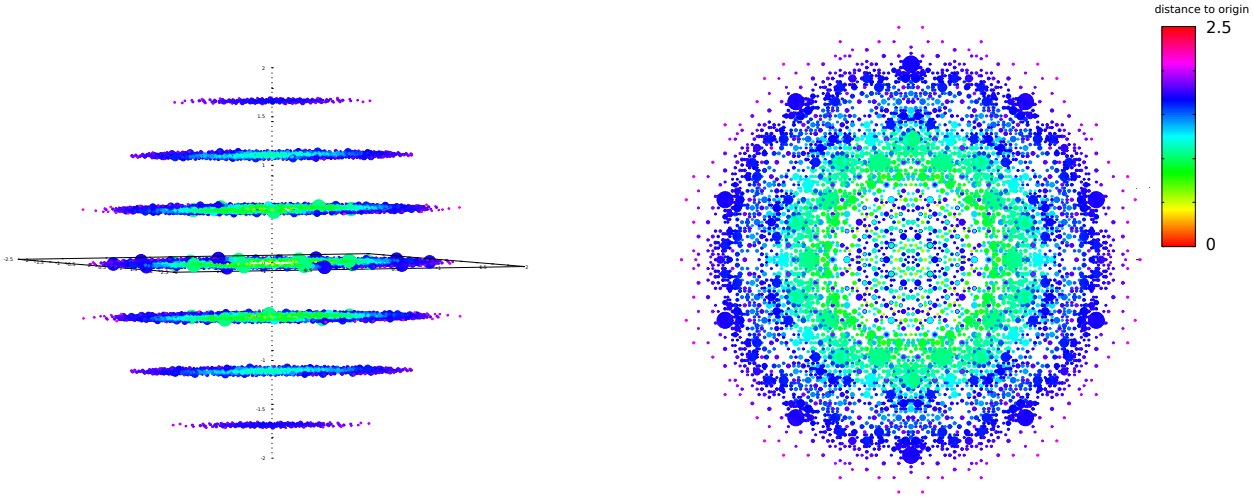

Figure 4.30: Stacked quasicrystal in Fourier space with a separation of layers of 0.553693

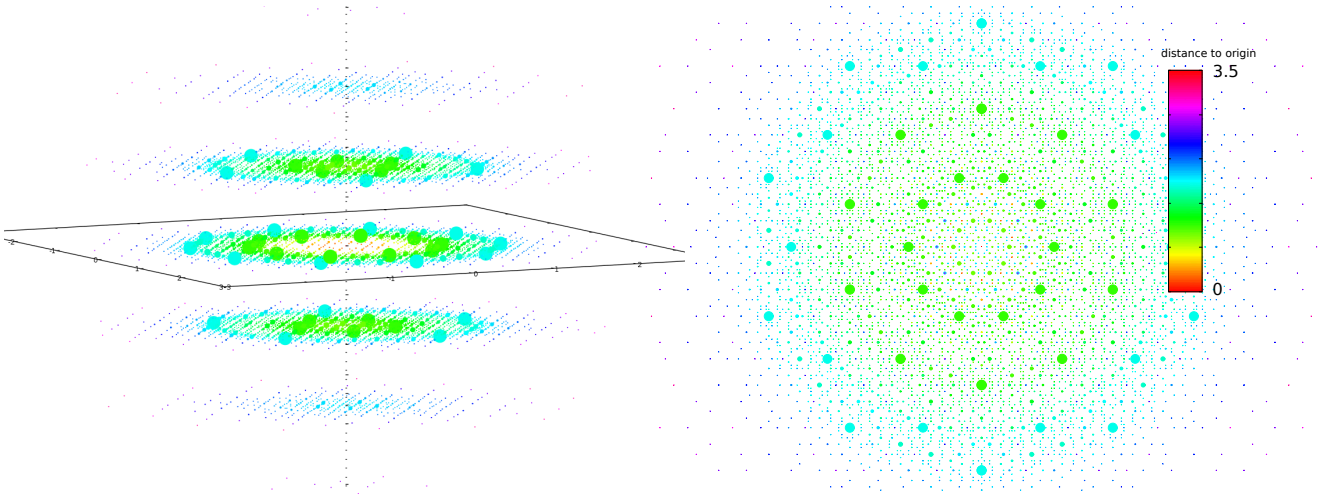

Figure 4.31: Stacked quasicrystal in Fourier space with a separation of layers of 0.89442

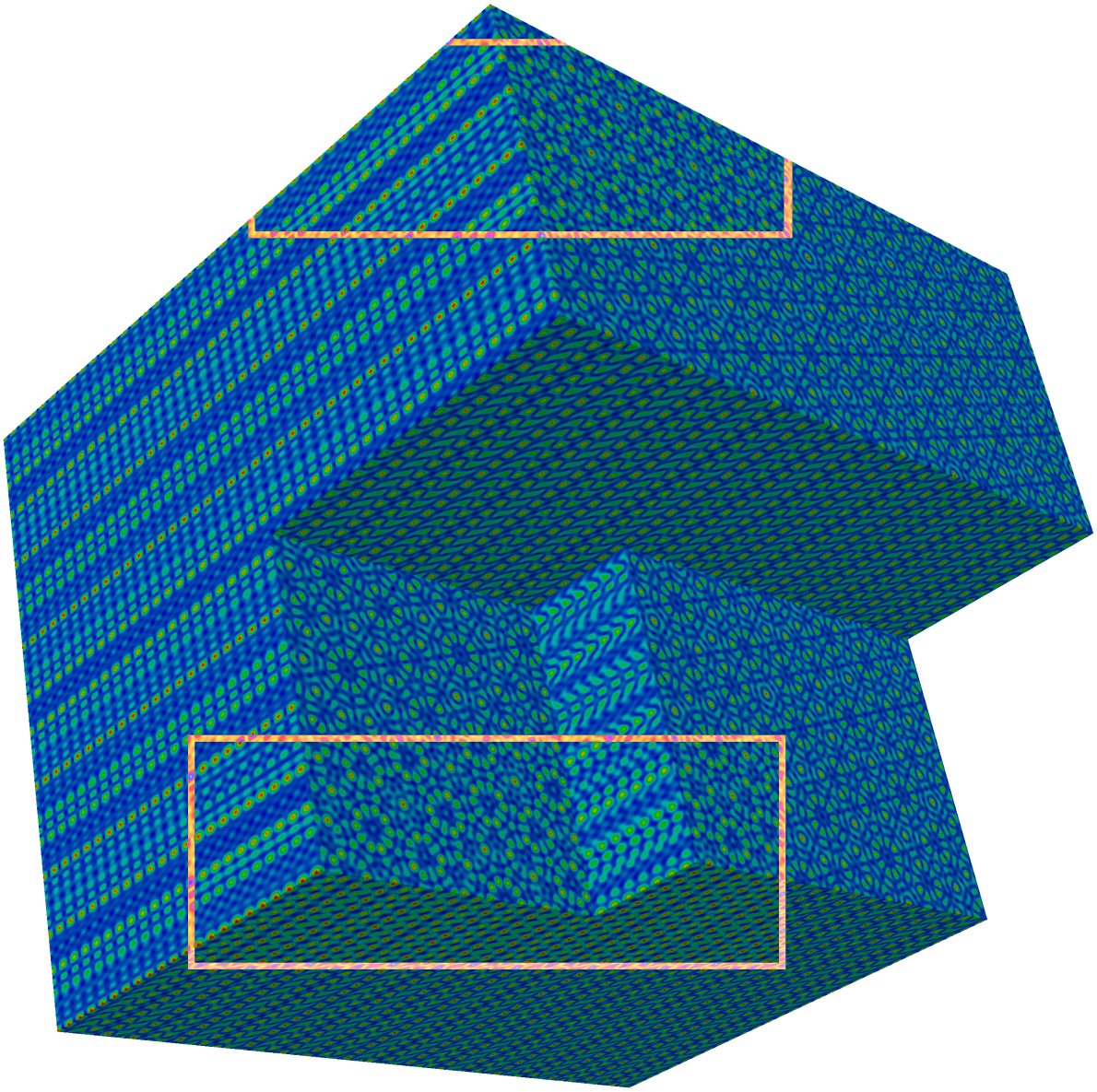

Figure 4.32: Real space image of stacked quasicrystal in figure 4.31 with a separation of layers of 0.89442 in Fourier space compared to its monomode approximation described in section 4.2.2.3. The main image shows the equilibrated structure. The monomode approximation is plotted inside the two red marked regions. The face shows the xy-plane with cuts through the structure at three different values of z.

Chapter 5

Outlook: Patchy Colloids

Some possible technological applications mentioned in the introduction in section 1.2 can only be realized with soft-matter systems. All models and results presented so far are based on an interaction potential with two incommensurate lengthscales. However, there are also other ways to realize quasicrystals in soft matter systems. A large variety of complex self-organized structures are observed in systems with so called *patchy colloids*. In this chapter constraints and requirements for extending the phase field crystal model of chapter 2 to patchy colloids are discussed.

5.1 Colloids with preferred angles

Colloids are particles that are dispersed in another phase, for example solid particles in a liquid solution. They can be used to study a large variety of phenomena in statistical physics including self-assembly and crystallization. The size of colloids is in the micrometer range. Patchy colloids usually carry attractive sites, sketched in figure 5.1 by blue dots. In experiments, such attractive sites can for example be realized by attaching short strands of DNA [6].

Figure 5.1: Schematic sketch of a patchy colloid with 5-fold rotation symmetry.

The forces between two colloids that carry such attractive sites are no longer isotropic. The colloids possess preferred binding angles just as many atoms do. In the following, a two dimensional system and particles with a fivefold rotation axis will be discussed, which could be used to construct colloidal quasicrystals comparable to figure 4.1 (e).

Compared to the model in chapter 2, particles with preferred binding angles are more than just a complementary approach. Due to their additional rotational degree of freedom there are more possibilities for ordered phases: A phase that has a constant density of particles but orientational order and a phase that has no orientational order but a non constant density distribution, as well as combinations of these two possibilities.

A phase field crystal model with orientational degree of freedom has already been derived and successfully used to model liquid crystals [22, 3]. The same model however cannot be used for quasicrystals with fivefold symmetry as in figure 5.1, because the free energy for the angular part assumes invariace for a rotation of π which is incompatible with $2\pi/5$.

5.2 Free Energy with orientational order

5.2.1 Introducing an order parameter for orientation

A free energy functional that only depends on one scalar order parameter ψ like the model in chapter 2 does not include any information about the orientational degree of freedom of patchy colloids. The model therefore has to be extended by introducing a new order parameter that depends on the particle's orientation angle φ with respect to a chosen director field. This new orientational order parameter will be called ψ_2 in the following. The order parameter ψ for the density distribution in this extended model is denoted as ψ_1. While ψ_1 is real, ψ_2 is a complex value $\psi_2 = |\psi_2| \exp(\mathrm{i}\varphi)$.

The free energy depends on both order parameters ψ_1 and ψ_2. It can be split into three groups:

$$F = F_{\psi_1} + F_{\psi_2} + F_{\psi_1\psi_2} \tag{5.1}$$

These are

- F_{ψ_1}: terms that only depend on the positional order parameter ψ_1.
- F_{ψ_2}: terms that only depend on the orientational parameter ψ_2.
- $F_{\psi_1\psi_2}$: mixing terms that depend on both ψ_1 and ψ_2.

The F_{ψ_1} and F_{ψ_2} group of terms depend on different order parameters. If the total free energy is invariant under a certain transformation, all three groups have to be invariant seperately. The F_{ψ_1} terms are equal to the terms calculated in section 2.3. The interesting term is the mixing term $F_{\psi_1\psi_2}$. In the following, we consider a Landau ansatz like described in section 2.3.1 to find an appropriate mixing term. The result proves that second order derivatives are not sufficient to model particles with fivefold rotational symmetry.

5.2.2 Finding rotation invariant terms

The most general mixing term $F_{\psi_1\psi_2}$ up to second order in the derivative is

$$F_{\psi_1\psi_2} = \left(v_0(\varphi) + v_1(\varphi)\,\partial_x + v_2(\varphi)\,\partial_y + v_3(\varphi)\,\partial_x^2 + v_4(\varphi)\,\partial_x\partial_y + v_5(\varphi)\,\partial_y^2\right)\psi_1 \tag{5.2}$$

where the coefficients v_i are arbitrary functions of the particles orientation angle φ that encode all information contained in the orientational order parameter ψ_2. Equation 5.2 uses cartesian coordinates. This choice of coordinates is not relevant to the problem. The same result can be derived using spherical coordinates or by reformulating the problem with directional derivatives

$$\partial_{\mathbf{e}_\phi} = \cos\phi\,\partial_x + \sin\phi\,\partial_y. \tag{5.3}$$

similar to [5]. For simplicity, equation 5.2 with cartesian coordinates will be used.

We will now reduce the number of coefficients by assuming rotational invariance of the entire system.

Testing the expression for rotation invariance means testing for invariance under the transformation

$$\partial_x \mapsto \partial_{x'} \tag{5.4}$$
$$\partial_y \mapsto \partial_{y'} \tag{5.5}$$
$$\varphi \mapsto \varphi + \theta \tag{5.6}$$

where the transformation of the partial derivatives is given by rotating the coordinate system. The rotation of the unit vectors e_x and e_y is

$$e_x = e_{x'} \cos\theta + e_{y'} \sin\theta \tag{5.7}$$
$$e_y = -e_{x'} \sin\theta + e_{y'} \cos\theta. \tag{5.8}$$

The gradient in cartesian coordinates is composed of partial derivatives. Replacing the unit vectors e_x and e_y with the expressions 5.7 and 5.8, the prefactors in front of the new basis vectors $e_{x'}$ and $e_{y'}$ can be set equal.

$$\nabla = \nabla' \tag{5.9}$$
$$e_x\partial_x + e_y\partial_y = e_{x'}\partial_{x'} + e_{y'}\partial_{y'} \tag{5.10}$$
$$= e_{x'}\left(\cos\theta\ \partial_x - \sin\theta\ \partial_y\right) + e_{y'}\left(\sin\theta\ \partial_x + \cos\theta\ \partial_y\right) \tag{5.11}$$

which translates to the relation for the partial derivatives

$$\partial_{x'} = \cos\theta\ \partial_x - \sin\theta\ \partial_y \tag{5.12}$$
$$(\partial_{x'})^2 = \cos^2\theta\ \partial_x^2 + \sin^2\theta\ \partial_y^2 - 2\sin\theta\cos\theta\ \partial_x\partial_y \tag{5.13}$$
$$\partial_{y'} = \sin\theta\ \partial_x + \cos\theta\ \partial_y \tag{5.14}$$
$$(\partial_{y'})^2 = \sin^2\theta\ \partial_x^2 + \cos^2\theta\ \partial_y^2 + 2\sin\theta\cos\theta\ \partial_x\partial_y \tag{5.15}$$
$$\partial_{x'}\partial_{y'} = \cos\theta\sin\theta\ (\partial_x^2 - \partial_y^2) + (\cos^2\theta - \sin^2\theta)\ \partial_x\partial_y \tag{5.16}$$

Looking at the transformation, one can see that the order of the derivative is conserved under the rotation. Thus, a 0th order derivative transforms into a 0th order derivative, a 1st order into a 1st order and a 2nd order into a 2nd order derivative. When transforming equation 5.2 this means that

$$v_0(\varphi) = v_0(\varphi + \theta) \tag{5.17}$$
$$v_1(\varphi)\ \partial_x + v_2(\varphi)\ \partial_y = v_1(\varphi+\theta)\ \partial_{x'} + v_2(\varphi+\theta)\ \partial_{y'} \tag{5.18}$$
$$v_3(\varphi)\ \partial_x^2 + v_4(\varphi)\ \partial_x\partial_y + v_5(\varphi)\ \partial_y^2 = v_3(\varphi+\theta)\ \partial_{x'}^2 + v_4(\varphi+\theta)\ \partial_{x'}\partial_{y'} + v_5(\varphi+\theta)\ \partial_{y'}^2. \tag{5.19}$$

For the 0th order equation 5.17 the coefficient function v_0 is simply a constant. Substituting the results for the first derivatives, equations 5.12 and 5.14 into the first order equation 5.18 one gets the relations

$$v_1(\varphi) = \cos\theta\ v_1(\varphi+\theta) + \sin\theta\ v_2(\varphi+\theta) \tag{5.20}$$
$$v_2(\varphi) = -\sin\theta\ v_1(\varphi+\theta) + \cos\theta\ v_2(\varphi+\theta) \tag{5.21}$$

which is a rotation of the vector (v_1, v_2) by the angle θ. The non-trivial solution is of the form $(v_1, v_2)(\varphi) := (\cos\varphi, \sin\varphi)$, where an arbitrary phase shift that is equivalent to the chosen director field can be added to φ. In the same way as the 1st derivative, the relation for the 2nd derivative

can also be written in matrix form by taking the vector $\mathbf{v} = (v_3, v_4, v_5)$:

$$\mathbf{v}(\varphi) = M(\theta)\mathbf{v}(\varphi + \theta) \tag{5.22}$$

Substituting in the relations 5.13, 5.15 and 5.16 into the third order equation 5.19, the transformation matrix becomes

$$M(\theta) = \begin{pmatrix} \cos^2\theta & -\frac{1}{2}\sin 2\theta & \sin^2\theta \\ -\sin 2\theta & \cos 2\theta & -\sin 2\theta \\ \sin^2\theta & \frac{1}{2}\sin 2\theta & \cos^2\theta \end{pmatrix} \tag{5.23}$$

The matrix M can be diagonalized using a matrix S that is composed of the eigenvectors of M:

$$M\mathbf{v}(\varphi) = \mathbf{v}(\varphi + \theta) \tag{5.24}$$
$$S\tilde{M}S^{-1}\mathbf{v}(\varphi) = \mathbf{v}(\varphi + \theta) \tag{5.25}$$
$$\tilde{M}S^{-1}\mathbf{v}(\varphi) = S^{-1}\mathbf{v}(\varphi + \theta) \tag{5.26}$$
$$\tilde{M}\tilde{\mathbf{v}}(\varphi) = \tilde{\mathbf{v}}(\varphi + \theta). \tag{5.27}$$

With the eigenvector matrix S, the diagonalized matrix $\tilde{M}$ and the inverse of the matrix S

$$S = \begin{pmatrix} 1 & -1 & -1 \\ 0 & -2\mathrm{i} & 2\mathrm{i} \\ 1 & 1 & 1 \end{pmatrix} \tag{5.28}$$
$$\tilde{M} = \mathrm{diag}(1, \cos(2\theta) - \mathrm{i}\sin(2\theta), \cos(2\theta) + \mathrm{i}\sin(2\theta)) \tag{5.29}$$
$$S^{-1} = \frac{1}{4}\begin{pmatrix} 2 & 0 & 2 \\ -1 & \mathrm{i} & 1 \\ -1 & -\mathrm{i} & 1 \end{pmatrix} \tag{5.30}$$

the transformed vector $\tilde{\mathbf{v}}$ can be given in terms of the original vector components (v_1, v_2, v_3):

$$\tilde{\mathbf{v}} = S^{-1}\mathbf{v} = \frac{1}{4}\begin{pmatrix} 2v_1 + 2v_3 \\ -v_1 + \mathrm{i}v_2 + v_3 \\ -v_1 - \mathrm{i}v_2 + v_3 \end{pmatrix} \tag{5.31}$$

Substituting this into the equation 5.27 leads results in the following set of equations

$$(v_1 + v_3)(\varphi) = (v_1 + v_3)(\varphi + \theta) \tag{5.32}$$
$$(-v_1 + \mathrm{i}v_2 + v_3)(\varphi) \cdot e^{-\mathrm{i}2\theta} = (-v_1 + \mathrm{i}v_2 + v_3)(\varphi + \theta) \tag{5.33}$$
$$(-v_1 - \mathrm{i}v_2 + v_3)(\varphi) \cdot e^{+\mathrm{i}2\theta} = (-v_1 - \mathrm{i}v_2 + v_3)(\varphi + \theta) \tag{5.34}$$

The first equation 5.32 can only be fulfilled if $(v_1 + v_3)$ is constant. Taking the last two equations 5.34 and 5.33, one can substitute $(-v_1 - \mathrm{i}v_2 + v_3)$ with a complex function that has an amplitude r and phase ϑ. Both depend on the angle given as an argument to the function. The equations simplify, leaving

$$r(\varphi) \cdot e^{\mathrm{i}(\vartheta(\varphi)+2\theta)} = r(\varphi + \theta) \cdot e^{\mathrm{i}\vartheta(\varphi+\theta)} \tag{5.35}$$
$$\vartheta(\varphi) + 2\theta = \vartheta(\varphi + \theta) \bmod 2\pi \tag{5.36}$$
$$\vartheta(\varphi) = 2\varphi \bmod 2\pi \tag{5.37}$$

where the amplitude function r has to be constant. Using equations 5.34 and 5.33 and the relation $v_3 = -v_1 + \text{const.}$ obtained from equation 5.32 leads to

$$(2v_1 + \mathrm{i}v_2)(\varphi) = r \cdot e^{\mathrm{i}2\varphi} \tag{5.38}$$

and the resulting coefficient vector

$$(v_1, v_2, v_3)(\varphi) = \tfrac{r}{2} \left(\cos 2\varphi, 2\sin 2\varphi, -\cos 2\varphi\right). \tag{5.39}$$

Putting together the solution for 0th, 1st and 2nd derivative terms, the final result for rotation invariant mixed terms is

$$F_{\psi_1\psi_2} = \left(v_0 + v_1 \left(\cos\varphi\, \partial_x + \sin\varphi\, \partial_y\right) + v_3 \left(\cos 2\varphi\, \partial_x^2 + 2\sin 2\varphi\, \partial_x\partial_y - \cos 2\varphi\, \partial_y^2\right)\right) \psi_1 \tag{5.40}$$

where v_0, v_1 and v_3 are no longer functions, but constant parameters.

5.2.3 Expressing $F_{\psi_1\psi_2}$ in terms of ψ_1 and ψ_2

With an orientation order parameter field $\psi_2 = |\psi_2|e^{\mathrm{i}\varphi}$ the mixted term expression 5.40 can be reformulated as

$$F_{\psi_1\psi_2} = \Big(v_0 + v_1\big[\,\mathrm{Re}(\psi_2)\partial_x + \mathrm{Im}(\psi_2)\partial_y\big] + \tilde{v}_3\big[\,\mathrm{Re}(\psi_2\psi_2)(\partial_x^2 - \partial_y^2) + 2\,\mathrm{Im}(\psi_2\psi_2)\partial_x\partial_y\big]\Big)\psi_1 \tag{5.41}$$

which is identical to the free energy used in [3] for liquid crystals with inversion symmetry. Due to this symmetry, it cannot model particles with fivefold rotational symmetry.

The correspondence of the order of the derivative to the prefactor of the angle, demonstrated here for derivatives of second order leads to the conclusion that the highest order terms in a free energy functional for patchy colloids with fivefold symmetry need to be of $\mathcal{O}(\psi^{10})$.

Chapter 6

Summary and Conclusions

It has been demonstrated that phase field crystal models can be used for calculating phases in three dimensions and that it is possible to adapt them for modeling quasicrystals. Several different methods were successfully employed in order to calculate quasicrystalline phases in two dimensional space and model their dynamics. It was shown that the same setup can be adapted to study three dimensional phases.

A rough overview for the phase space in three dimensions was given, as well as several examples for stable and metastable three dimensional structures that were encountered, including two variants of stacked quasicrystals. Several different monomode approximations with icosahedral symmetry were compared and used as initial conditions for the minimization. Furthermore, an example for results obtained with growing two dimensional quasicrystals in three dimensions was presented.

Finally, it was shown that with the methods and parameters used for two dimensional quasicrystals it is not possible to obtain quasicrystals with icosahedral symmetry in three dimensional space.

For both simulations and experiments, it would be desirable to have alternative methods to grow quasicrystals, making the outcome less sensitive to special initial conditions. One alternative method has been discussed. It is not based on interaction potentials with two incommensurate lengthscales, but uses preferred binding angles instead. For this method it was shown that phase field crystal model based approaches with second order directional derivatives are not sufficient for fivefold symmetry. For the future, such models could be realized by using 10th order directional derivatives.

Bibliography

[1] (1992). Report of the Executive Committee for 1991. *Acta Crystallographica Section A*, 48(6):922–946.

[2] Achim, C. V., Schmiedeberg, M., and Löwen, H. (2014). Growth modes of quasicrystals. *Phys. Rev. Lett.*, 112:255501.

[3] Achim, C. V., Wittkowski, R., and Löwen, H. (2011). Stability of liquid crystalline phases in the phase-field-crystal model. *Phys. Rev. E*, 83:061712.

[4] Barkan, K., Diamant, H., and Lifshitz, R. (2011). Stability of quasicrystals composed of soft isotropic particles. *Phys. Rev. B*, 83:172201.

[5] Belyaev, A., Khesin, B., and Tabachnikov, S. (2012). Discrete spherical means of directional derivatives and veronese maps. *Journal of Geometry and Physics*, 62(1):124 – 136.

[6] Bianchi, E., Blaak, R., and Likos, C. N. (2011). Patchy colloids: state of the art and perspectives. *Phys. Chem. Chem. Phys.*, 13:6397–6410.

[7] Childs, H., Brugger, E., Whitlock, B., Meredith, J., Ahern, S., Pugmire, D., Biagas, K., Miller, M., Harrison, C., Weber, G. H., Krishnan, H., Fogal, T., Sanderson, A., Garth, C., Bethel, E. W., Camp, D., Rübel, O., Durant, M., Favre, J. M., and Navrátil, P. (2012). VisIt: An End-User Tool For Visualizing and Analyzing Very Large Data. In *High Performance Visualization–Enabling Extreme-Scale Scientific Insight*, pages 357–372.

[8] Damasceno, P. F., Glotzer, S. C., and Engel, M. (2017). Non-close-packed three-dimensional quasicrystals. *J. Phys.: Condens. Matter*, 29(23):234005.

[9] Deffeyes, K. and Deffeyes, S. (2009). *Nanoscale: Visualizing an Invisible World*. MIT Press.

[10] Dubois, J.-M. (2012). Properties- and applications of quasicrystals and complex metallic alloys. *Chem. Soc. Rev.*, 41:6760–6777.

[11] Dunlap, R. A. (1997). *The Golden Ratio And Fibonacci Numbers*. World Scientific Publishing Company.

[12] Elder, K. R., Katakowski, M., Haataja, M., and Grant, M. (2002). Modeling elasticity in crystal growth. *Phys. Rev. Lett.*, 88:245701.

[13] Emmerich, H., Löwen, H., Wittkowski, R., Gruhn, T., Tóth, G. I., Tegze, G., and Gránásy, L. (2012). Phase-field-crystal models for condensed matter dynamics on atomic length and diffusive time scales: an overview. *Adv. Phys.*, 61(6):665–743.

[14] Frigo, M. and Johnson, S. G. (2005). The design and implementation of FFTW3. *Proc. IEEE*, 93(2):216–231. Special issue on "Program Generation, Optimization, and Platform Adaptation".

[15] Geyer, D. (2017). Aktives Phasenfeldkristall-Modell für biologische Systeme. Bachelor thesis, Friedrich Alexander Universität Erlangen-Nürnberg.

[16] Hahn, T., editor (1992). *International Tables For Crystallography.* Kluwer Academic Publishers.

[17] Hargittai, I. (1990). *Quasicrystals, Networks, and Molecules of Fivefold Symmetry.* VCH-Verlag-Ges.

[18] Jaatinen, A., Achim, C. V., Elder, K. R., and Ala-Nissila, T. (2009). Thermodynamics of bcc metals in phase-field-crystal models. *Phys. Rev. E*, 80:031602.

[19] Jaric, M., editor (2012). *Introduction to quasicrystals.* Elsevier.

[20] Levine, D. and Steinhardt, P. J. (1986). Quasicrystals. i. definition and structure. *Phys. Rev. B*, 34:596–616.

[21] Lifshitz, R. and Petrich, D. M. (1997). Theoretical model for faraday waves with multiple-frequency forcing. *Phys. Rev. Lett.*, 79:1261–1264.

[22] Löwen, H. (2010). A phase-field-crystal model for liquid crystals. *Journal of Physics: Condensed Matter*, 22(36):364105.

[23] Rechtsman, M. C., Jeong, H.-C., Chaikin, P. M., Torquato, S., and Steinhardt, P. J. (2008). Optimized structures for photonic quasicrystals. *Phys. Rev. Lett.*, 101:073902.

[24] Rottler, J., Greenwood, M., and Ziebarth, B. (2012). Morphology of monolayer films on quasicrystalline surfaces from the phase field crystal model. *J. Phys.: Condens. Matter*, 24(13):135002.

[25] Shechtman, D., Blech, I., Gratias, D., and Cahn, J. W. (1984). Metallic phase with long-range orientational order and no translational symmetry. *Phys. Rev. Lett.*, 53:1951–1953.

[26] Subramanian, P., Archer, A. J., Knobloch, E., and Rucklidge, A. M. (2016). Three-dimensional icosahedral phase field quasicrystal. *Phys. Rev. Lett.*, 117:075501.

[27] Swift, J. and Hohenberg, P. C. (1977). Hydrodynamic fluctuations at the convective instability. *Phys. Rev. A*, 15:319–328.

[28] Vardeny, Z. V., Nahata, A., and Agrawal, A. (2013). Optics of photonic quasicrystals. *Nat. Photonics*, 7(3):177–187.

Acknoledgements

This thesis would not be possible without the help of many people who supported me in various ways throughout the project.

First of all, I would like to thank my supervisors Michael Schmiedeberg for his continuous support, always providing helpful suggestions and feedback as well as Christian Achim, who taught me how to write the initial program, sharing with me various parts of code and scripts.

I would like to thank the administrators at Theorie-1 and at the RRZE for providing the computational resources used in this project and for their personal assistance in various software-related issues. In general I would like to thank the Theorie-1 chair and the group of Michael Schmiedeberg for the warm and welcoming atmosphere that made working a really enjoyable experience.

Eigenständigkeitserklärung

Hiermit versichere ich, dass ich die Masterarbeit selbstständig verfasst und keine anderen als die angegebenen Quellen und Hilfsmittel verwendet habe. Ich erkläre weiterhin, dass die vorliegende Arbeit noch nicht im Rahmen eines anderen Prüfungsverfahrens eingereicht wurde.

Erlangen den 3.5.2018